

1 **Magnetic record of deglaciation using FORC-PCA, sortable-silt grain size,**
2 **and magnetic excursion at 26 ka, from the Rockall Trough (NE Atlantic)**

3
4 J.E.T. Channell¹, R.J. Harrison², I. Lascu², I. N. McCave², F.D. Hibbert³, W.E.N. Austin^{4,5}

5
6 ¹Department of Geological Sciences, POB 112120, University of Florida, Gainesville, FL
7 32611 (USA)

8 ²Department of Earth Sciences, University of Cambridge, Cambridge, CB2 3EQ (UK)

9 ³Research School of Earth Sciences, Australian National University, Canberra, ACT 2601,
10 Australia

11 ⁴School of Geography and Geosciences, University of St. Andrews, St. Andrews, KY16 9AL
12 (UK)

13 ⁵Scottish Marine Institute, Scottish Association for Marine Science, Oban PA37 1QA, (UK)

14
15 Corresponding Author: J.E.T. Channell (jetc@ufl.edu, Tel: 352 392-3658)

16
17 **Abstract**

18 Core MD04-2822 from the Rockall Trough has apparent sedimentation rates of ~ 1 m/kyr
19 during the last deglaciation (Termination I). Component magnetization directions indicate a
20 magnetic excursion at 16.3 m depth in the core, corresponding to an age of 26.5 ka, implying
21 an excursion duration of ~350 years. Across Termination I, the mean grain size of sortable silt
22 implies reduced bottom-current velocity in the Younger Dryas and Heinrich Stadial (HS)-1A,
23 and increased velocities during the Bølling-Allerød warm period. Standard bulk magnetic
24 parameters imply fining of magnetic grain size from the mid-Younger Dryas (~12 ka) until ~
25 8 ka. First-order reversal curves (FORCs) were analyzed using ridge extraction to differentiate
26 single domain (SD) from background (detrital) components. Principal component analysis
27 (FORC-PCA) was then used to discriminate three end members corresponding to SD, pseudo-

28 single domain (PSD) and multidomain (MD) magnetite. The fining of bulk magnetic grain
29 size from 12 to 8 ka is due to reduction in concentration of detrital (PSD+MD) magnetite,
30 superimposed on a relatively uniform concentration of SD magnetite produced by
31 magnetotactic bacteria. The decrease in PSD+MD magnetite concentration from 12 to 8 ka is
32 synchronized with increase in benthic $\delta^{13}\text{C}$, and with major (~70 m) regional sea-level rise,
33 and may therefore be related to detrital sources on the shelf that had reduced influence as sea
34 level rose, and to bottom-water reorganization as Northern Source Water (NSW) replaced
35 Southern Source Water (SSW).

36

37 **1. Introduction**

38 Core MD04-2822 from the Rockall Trough (Fig. 1), collected from the RV *Marion*
39 *Dufresne* in 2004, is ~37 m long and extends back to ~195 ka (Hibbert et al., 2010).
40 Sedimentation rates are highly variable, declining to <5 cm/kyr in marine isotope stage (MIS)
41 5, but exceeding 1 m/kyr in MIS 2 and the transition into the Holocene (Termination I),
42 although apparent sedimentation rates may be influenced by “stretching” that affects the
43 upper part of the majority of MD (*Marion Dufresne*) cores (Skinner and McCave, 2003;
44 Széréméta et al., 2004). Core MD04-2822 is from the distal margin of the Barra-Donegal fan
45 (56° 50.54 N, 11° 22.96 W, 2344 m water depth). The Barra-Donegal Fan is the most
46 southerly glacial fan on the NW European continental margin comprising debris flow lobes
47 and glaciomarine sediments fed by Pleistocene ice streams (Stoker 1995; Armishaw et al.,
48 2000; Knutz et al., 2001). Deep ocean circulation in this region changed during Termination I
49 as Southern Source Water (SSW) reached water depths as shallow as ~2000 m during the Last
50 Glacial Maximum (LGM) (Curry and Oppo, 2005), and was replaced during Termination I by

51 North East Atlantic Deep Water (NEADW) with a component of Wyville-Thomson Ridge
52 Overflow Water (WTOW) and Labrador Sea Water (LSW) (Fig. 1). Southern Source Water
53 (SSW) is found today in the deepest portion of the Trough (below 3000 m) with a pronounced
54 vertical silicate gradient denoting the mixing of underlying SSW with NEADW, and
55 superimposed southwesterly flow of WTOW along the western side Rockall Trough (New
56 and Smythe-Wright, 2001). Core MD04-2822 comprises clays and silts with minor sand
57 (Hibbert et al., 2010). The attraction of this core for magnetic studies lies in its precise
58 chronology, based on radiocarbon, tephra, benthic $\delta^{18}\text{O}$, and correlation of sea-surface
59 temperature (SST) proxies to ice-core records, as well as the relatively high sedimentation
60 rates in MIS 2 and during Termination I.

61 Variations in magnetic concentration parameters in North Atlantic sediments deposited
62 over the last glacial cycle have been have been attributed to changes in transport of magnetic
63 particles by deep-sea currents (e.g., Kissel et al., 1999). A north to south reduction in both
64 magnetic concentration and magnetic grain size in Holocene sediments along the axis of the
65 Gardar/Bjorn drifts, over a distance of ~2000 km, has been attributed to down-stream
66 transport of magnetic particles by deep-sea currents flowing from detrital sources along the
67 Iceland-Scotland ridge (Kissel et al., 2009). Also in Holocene sediments from the Gardar
68 Drift, magnetic susceptibility tracks the mean grain size of sortable silt, implying that
69 magnetic susceptibility in this region is a monitor of bottom-current strength (Kissel et al.,
70 2013). Similarly, Snowball and Moros (2003) found that magnetic concentration and grain
71 size over the last glacial cycle from the central Gardar Drift, track the means of the 0.5-10 μm
72 and 0.5-20 μm particle size fractions, again implying a link between magnetic concentration,
73 magnetic grain size, and bottom-current velocity.

74 Here we report the natural remanent magnetization (NRM), including the presence of a
75 magnetic excursion at ~26 ka, and magnetic and physical granulometry, of Core MD04-2822.
76 Measurements are from u-channel samples, continuous 2x2x150 cm³ samples encased in
77 plastic with a clip-on lid constituting one of the sides, collected from each (150-cm) core
78 section. In addition, 7-cm³ discrete samples were collected across the supposed magnetic
79 excursion, and toothpick samples for magnetic hysteresis measurements and First-Order
80 Reversal Curves (FORCs) were collected throughout the section but particularly over
81 Termination I.

82 This study represents the first application of FORC-PCA, a new method of magnetic
83 unmixing that uses principle component analysis (PCA) applied to FORC diagrams. We
84 compare this method with more traditional magnetic grain size proxies, and demonstrate that
85 FORC-PCA leads to an improved understanding of how magnetic variations are linked to
86 underlying geological processes. The results contribute to the controversial issue of the age
87 and existence of magnetic excursions younger than the Laschamp excursion at ~41 ka, and
88 provide a new perspective on the relationship between magnetic and physical grain size in
89 North Atlantic sediments over the last glacial cycle.

90

91 **2. Age Model**

92 The chronology of Core MD04-2822 was originally based on AMS radiocarbon dates,
93 benthic $\delta^{18}\text{O}$ from *Cibicides wuellerstorfi*, and percent *Neogloboquadrina pachyderma*
94 (sin.) as a sea-surface temperature (SST) proxy linked to the Greenland $\delta^{18}\text{O}$ and Antarctic
95 methane records (Hibbert et al., 2010). The age model has now been strengthened by: (1)
96 recognition of both the Vedde Ash (I-RHY-I component) at 12.17 ka and North Atlantic Ash

97 Zone (NAAZ) II at 55.38 ka. (2) Use of percent *N. pachyderma* (sin.) to link the core to
98 Greenland ice core (NGRIP) $\delta^{18}\text{O}$, using updated ages for the NGRIP ice core on the GICC05
99 timescale (Rasmussen et al., 2014 and references therein), and beyond 140 ka, the use of the
100 Antarctic AICC2012 chronology for the EDC ice core (Bazin et al., 2013) to perform this
101 linkage through methane tuning. (3) Additional AMS ^{14}C dating (Austin and Hibbert, 2012;
102 Hibbert et al., 2014; Table S1) calibrated using the Marine13 calibration curve (Reimer et al.,
103 2013) using OxCal (version 4.2; Bronk Ramsey, 2009). We use $\Delta R = 0 \pm 50$ to calibrate the
104 Holocene samples, at present, the average (n=6) regional $\Delta R = -1 \pm 52$ (Harkness, 1983;
105 Håkansson, 1984; Olsson, 1980). Locally, the marine reservoir increased to 700 years
106 (Austin et al., 1995) during the Younger Dryas, with glacial values of >1000 years proposed
107 (cf. Waelbroeck et al., 2001). We used $\Delta R = 700 \pm 500$ for the single *N. pachyderma* (sin.)
108 date (SUERC 12920) to account for changes in glacial surface oceanography. The similarity
109 of the radiocarbon determinations from the upper 15.5 cm of the core (Table S1) results from
110 the biological mixing of sediments. Consequently, we set the bottom of the surface mixed
111 layer (i.e. the limit of the biologically mixed layer) to a depth of 15.5 cm for MD04-2822 with
112 an age derived from the average of three calibrated ^{14}C dates (cf. Brown et al., 2001). Age
113 uncertainty estimates (Fig. S1, Tables S1 and S2) were determined for each tie-point using a
114 mean squared estimate that included age uncertainties associated with ice-core chronologies,
115 and the error in the position of the tie-point within the marine record due to sample spacing,
116 core resolution, and sediment bioturbation. We combined the tie-point age and depth
117 information using a Bayesian deposition model (the OxCal ‘Poisson’ function, allowing
118 sedimentation rates to vary widely; Bronk Ramsey and Lee, 2013) to derive age control
119 between tie-points. The overall agreement between the model priors and posteriors is high:

120 agreement index > 78 % for all dates in the MD04-2822 Poisson model (acceptance threshold
121 > 60%; Bronk Ramsey, 2008). Sedimentation rates are highly variable with sedimentation rate
122 maxima in MIS 2 and across Termination I (Fig. 2).

123

124 **3. Magnetic methods**

125 Continuous u-channel samples were collected from the 1.5 m-long archive-half sections
126 of Core MD04-2822. Measurements of natural remanent magnetization (NRM) of u-channel
127 samples were made at 1-cm intervals, with a 10-cm leader and trailer at the top and base of
128 each u-channel sample, using a 2G Enterprises pass-through magnetometer at the University
129 of Florida that has Gaussian-shaped response functions with width at half-height of ~4.5 cm
130 (Weeks et al., 1993; Guyodo et al., 2002). After initial NRM measurement of u-channel
131 samples, stepwise alternating field (AF) demagnetization was carried out in 5 mT increments
132 in the 10-60 mT peak field interval, and in 10 mT increments in the 60-100 mT interval, using
133 tracking speeds of 10 cm/s. Component magnetizations were computed each 1-cm for a
134 uniform 20-80 mT demagnetization interval using the standard least-squares method
135 (Kirschvink, 1980) without anchoring to the origin of the orthogonal projections, using
136 UPmag software (Xuan and Channell, 2009).

137 The apparent excursion recorded in the u-channel record of Core MD04-2822 was also
138 sampled using cubic (7 cm³) plastic boxes, collected from alongside the u-channel trough, in
139 order to further investigate the excursion interval. Discrete samples were subject to either
140 stepwise alternating field (AF) or thermal demagnetization after initial measurement of NRM.
141 For AF demagnetization, increments were 5 mT in the 5-95 mT peak AF range. Thermal
142 demagnetization experiments were conducted by measuring NRM before thermal

143 demagnetization, then again after wrapping samples in Al foil, and then after demagnetization
144 of wrapped samples in 25 °C steps in the 75-600°C temperature range. Magnetization
145 directions were measured on a 2G Enterprises discrete-sample magnetometer, and component
146 magnetization directions were determined using at least ten concurrent demagnetization steps
147 without anchoring to the origin of the orthogonal projections. After AF demagnetization of
148 the NRM of 7-cm³ discrete samples recording the apparent magnetic excursion (Fig. 5), these
149 40 samples were dried in field-free space, extracted from their plastic cubes, and wrapped in
150 Al-foil. The remanent magnetization was measured before and after wrapping, and then 3-axis
151 IRMs were imposed sequentially and orthogonally for each sample using DC fields of 0.1 T,
152 0.3 T and 1.2 T (see Lowrie, 1990).

153 After NRM measurement of u-channel samples, anhysteretic remanent magnetization
154 (ARM) was imposed on each u-channel in a DC field of 50 μ T and an AF field decaying from
155 a peak value of 100 mT, and then this ARM was demagnetized at the same steps used to
156 demagnetize NRM. The slope of NRM versus ARM during stepwise demagnetization was
157 used as a proxy for relative paleointensity (RPI), the intensity of the geomagnetic field at time
158 of sediment deposition. This RPI proxy was augmented by two additional proxies (slopes),
159 also measured at 1-cm intervals down-core: NRM demagnetization versus ARM acquisition
160 (ARMAQ), and NRM demagnetization versus demagnetization of isothermal remanent
161 magnetization (IRM) acquired in a DC field of 1T (e.g., Channell et al., 2014). Ideally, ARM
162 and IRM activate the same population of magnetite grains that carry NRM, and hence
163 normalizes NRM intensity for changes in the concentration of NRM-carrying grains down-
164 core. Volume susceptibility (κ) was measured at 1-cm intervals using a susceptibility track
165 designed for u-channel samples that has a Gaussian-shaped response function, with width at

166 half height of ~ 4 cm, similar to the response function of the u-channel magnetometer (Thomas
167 et al., 2003). Following Banerjee et al. (1981) and King et al. (1983), the ratio of anhysteretic
168 susceptibility (κ_{ARM} , ARM intensity normalized by the DC bias field used to acquire the
169 ARM) to susceptibility (κ) can be used to estimate grain size in magnetite. The measurement
170 of IRM, acquired in DC fields of 0.3 T and 1 T ($\text{IRM}_{0.3\text{T}}$ and $\text{IRM}_{1\text{T}}$), allows us to calculate a
171 “forward S-ratio” (see Heslop, 2009) calculated as the ratio: $\text{IRM}_{0.3\text{T}} / \text{IRM}_{1\text{T}}$. The S-ratio is
172 sensitive to the abundance of high-coercivity minerals such as hematite and is not primarily
173 influenced by magnetic grain-size.

174 Additional mineralogical information was acquired from magnetic hysteresis data
175 measured on a Princeton Measurements Corp. vibrating sample magnetometer (VSM) at the
176 University of Florida. Hysteresis ratios: M_r/M_s and B_{cr}/B_c where M_r is saturation remanence,
177 M_s is saturation magnetization, B_{cr} is coercivity of remanence, and B_c is coercive force, can be
178 used to delineate single domain (SD), pseudo-single domain (PSD) and multidomain (MD)
179 magnetite and to assign “mean” magnetite grain sizes through empirical and theoretical
180 calibrations of the so-called Day plot (Day et al., 1977; Carter-Stiglitz et al., 2001; Dunlop,
181 2002; Dunlop and Carter-Stiglitz, 2006). First order reversal curves (FORCs) provide
182 enhanced magnetic mineral and domain state discrimination (Pike et al., 1999; Roberts et al.,
183 2000; Muxworthy and Roberts, 2007) and are measured by progressively saturating a small
184 (few hundred mg) sample in a field (B_{sat}), decreasing the field to a value B_a , reversing the
185 field and sweeping it back to B_{sat} in a series of regular field steps (B_b). The process is repeated
186 for many values of B_a . The magnetization is then represented as a contour plot with axes B_c
187 and B_u where $B_c = (B_b - B_a)/2$ and $B_u = (B_b + B_a)/2$. The contoured distribution of a FORC can be
188 interpreted in terms of the coercivity distribution along the B_c axis. Spreading of the

189 distribution along the B_u axis corresponds to magnetostatic interactions for SD grains or
190 internal demagnetizing fields for MD grains, although the latter dominates in weakly
191 magnetized deep-sea sediments, and spreading in B_u combined with low B_c can be interpreted
192 in terms of high MD magnetite content. In general, closed peaked structures along the B_c axis
193 are characteristic of SD grains, with contours becoming progressively more parallel to the B_u
194 axis with grain-size coarsening. FORC diagrams were mass normalized and processed with
195 FORCinel (Harrison and Feinberg, 2008) using drift correction and VARIFORC smoothing
196 protocols described by Egli (2013). Two hundred and thirteen (213) FORCs collected at 2-5
197 cm intervals over the 4.5-18.5 ka interval were measured using averaging time of 1 s, and a
198 field increment of 2 mT up to a maximum applied field of 1 T. FORCs were analyzed by two
199 methods: (1) by extraction of the ridge (SD) signal and interpolation of the background,
200 followed by subtraction of the background from the total FORC signal, following Egli et al.
201 (2010), and (2) by Principal Component Analysis (PCA) following Lascau et al. (2015).
202 FORCs were mass normalized and smoothed using $S_{c0} = 7$, $S_{c1} = 9$, $S_{b0} = 3.5$, $S_{b1} = 9$, $\lambda_c = 0.1$,
203 $\lambda_b = 0.1$.

204

205 **4. Magnetic excursion at ~26 ka**

206 The maximum angular deviation (MAD) values associated with NRM component
207 magnetization directions are generally below 10° for Core MD04-2822 (Fig. 3), indicating
208 well-defined magnetization components. Cores were not oriented in azimuth although
209 declination is relative as the same (archive) half of the core was consistently sampled. The
210 high mean inclination ($\sim 68^\circ$), close to that expected for a geocentric axial dipole field at the
211 sampling site (72°), results in high variation in declination, superimposed on apparent twisting

212 of the sediment core. An apparent magnetic excursion is observed in declination and
213 inclination at ~16 meters below seafloor (mbsf) (Fig. 3).

214 Magnetic excursions are brief (millennial-scale) directional aberrations of the
215 geomagnetic field that, when optimally recorded, are often manifested as paired reversals
216 where the virtual geomagnetic poles (VGPs) reaches high latitudes in the opposite hemisphere
217 (Laj and Channell, 2007; Channell et al., 2012). Magnetic excursions coincide with relative
218 paleointensity (RPI) minima, as do long-lived reversals, and ~8 excursions have been
219 adequately documented within the Brunhes Chron (e.g., Laj and Channell, 2007). The catalog
220 of Quaternary magnetic excursions is controversial for several reasons. Magnetic excursions
221 are brief millennial- or centennial-scale events and therefore their recording is fortuitous in
222 sediments or volcanic rocks, and depends on the stochastic nature of sediment accumulation
223 or volcanic eruption. Magnetic excursions are only likely to be recorded in sediments with
224 mean sedimentation rates well in excess of 10 cm/kyr. The recording of such brief events in
225 sediments is “filtered” by the NRM acquisition process, which results in smoothing of the
226 signal through bioturbation in the uppermost ~10 cm, and progressive remanence acquisition
227 below the bioturbated layer (see Channell and Guyodo, 2004; Roberts and Winklhofer, 2004;
228 Stoner et al., 2013). In addition, age dating of putative excursions is often not sufficiently
229 robust to distinguish one excursion from another, and to conclusively ascertain that repeated
230 observations are unequivocal observations of the same event. Furthermore, directional
231 anomalies in NRM data may be accounted for by a myriad of non-geomagnetic causes,
232 including drilling and sampling disturbance.

233 Typical orthogonal projections of demagnetization data recording the magnetic excursion
234 from u-channel samples (AF demagnetization) and discrete samples (thermal and AF

235 demagnetization) are illustrated in Figure 4. All orthogonal projections in Figure 4, other than
236 Fig. 4f that is an example from just above the excursion interval, show magnetization
237 components with steep negative inclinations, implying the presence of the magnetic
238 excursion. Across the excursion interval, component magnetization directions from u-channel
239 samples, computed for a uniform 20-60 mT peak demagnetizing field, are associated with
240 MAD values that are generally lower than MAD values associated with discrete samples (Fig.
241 5), probably due to the averaging effect of the larger (u-channel) magnetometer response
242 function and/or to increased sediment disturbance associated with discrete sampling.
243 Nonetheless, MAD values are predominantly $<10^\circ$ indicating moderately well-defined
244 component magnetizations for both discrete and u-channel samples (Fig. 5). Excursion
245 component directions are observed over a ~ 35 cm interval from 1615-1650 cmbsf or 26.35-
246 26.70 ka, an excursion duration of ~ 350 years according to the age model. Virtual
247 geomagnetic poles (VGPs) reach high (negative) latitudes in the southern hemisphere (Fig. 5)
248 implying that the excursion apparently involves reversal of the Earth's main dipole field. The
249 VGP path involves three loops, two of which precede the loop (Loop 3 in Figure 5) that takes
250 the VGPs to highly southerly latitude.

251 The apparent magnetic excursion lies within a RPI minimum in Core MD04-2822 that is
252 defined by three RPI proxies: slopes of NRM/ARM, NRM/ARMAQ and NRM/IRM (Fig.
253 6a). RPI minima at ~ 16.3 , ~ 19.4 , and ~ 20.6 mbsf (shaded in Fig. 6a) correspond to ages of
254 26.5, 34.5 and 40.8 ka (shaded in Fig. 6b). RPI data have lower resolution below 18 mbsf (29
255 ka) due to reduced sedimentation rates below 18 mbsf (29 ka) relative to the section above
256 (Fig. 2). Calibrated RPI templates, such as PISO that covers the last 1.5 Myr (Channell et al.,
257 2009), have inadequate resolution for detailed comparison with the Core MD04-2822 RPI

258 record. On the other hand, RPI minima at ~34.5 and ~40.8 ka correspond to acceptable ages
259 for the Mono Lake and Laschamp excursions (Fig. 6b), respectively, and to RPI minima
260 derived from ice-core cosmogenic isotope flux (Muscheler et al., 2005).

261

262 **5. Magnetic mineralogy**

263 The mean of the S-ratio for Core MD04-2822 is 0.95 (std. deviations 0.05), indicating
264 that low coercivity magnetic minerals (e.g., magnetite) are dominant. The values of ($\kappa_{\text{ARM}}/\kappa$)
265 show a range of bulk magnetite grain size in the 0.1-5 μm range (Fig. 7a), according to the
266 calibration of King et al. (1983). By comparison with measurements of unannealed sized
267 magnetites (Dunlop, 2002), the Day plot indicates bulk magnetite grain sizes in the 0.1-5 μm
268 range (Fig. 7b), broadly consistent with the κ_{ARM} versus κ plot (Fig. 7a). The displayed FORC
269 diagram (Fig. 7c) is from the excursion interval, and is typical for the glacial intervals of the
270 core, and characterized by a mixture of SD and abundant detrital PSD+MD magnetite,
271 consistent with the Day plot (Fig. 7b). Thermal demagnetization of the 3-axis IRM, imposed
272 sequentially in DC fields of 1.2 T, 0.3 T and 0.1 T, indicates that the magnetic mineralogy is
273 dominated by a low-coercivity mineral that acquires its IRM in magnetizing fields of 0.1 T,
274 and that the IRMs do not have unblocking temperatures above 600°C (Fig. 7d), supporting the
275 dominance of magnetite in the magnetic mineralogy of the excursion interval.

276

277 **6. Magnetic and physical granulometry**

278 In Core MD04-2822, the Holocene and MIS 5 are associated with relatively fine
279 magnetite grain size, as indicated by the high values of the $\kappa_{\text{ARM}}/\kappa$ grain size parameter (Fig.
280 8). These changes in magnetic grain-size correspond with shifts in $\delta^{13}\text{C}$, and with Zr/Sr and

281 Si/Sr ratios determined by X-ray fluorescence (XRF) core scanning, that are proxies for
282 detrital input (e.g., Croudace et al., 2006). The $\kappa_{\text{ARM}}/\kappa$ grain-size parameter is, however,
283 lagged by a few kyr relative to $\delta^{18}\text{O}$ over Termination I and II (Fig. 8). The ARM/IRM ratio
284 (not shown) closely mimics the $\kappa_{\text{ARM}}/\kappa$ grain size parameter, indicating that the $\kappa_{\text{ARM}}/\kappa$ ratio
285 is not influenced by paramagnetic or diamagnetic contributions to susceptibility in these
286 magnetite-bearing sediments.

287 These observations led us to compare the parameter commonly used to gauge bottom-
288 current velocity, the mean sortable-silt (10-63 μm) grain size (McCave et al., 1995; McCave
289 et al., in prep.), with magnetic grain size and concentration parameters over Termination I
290 (Fig. 9). Samples were analyzed for particle size using a Coulter Multisizer 3 equipped with a
291 200 μm aperture giving an optimum sizing range of 4-80 μm . Prior to analysis, carbonate and
292 opaline silica were removed from the <63 μm grain-size fraction by treatment with dilute
293 acetic acid (1 M) and heated (85°C) sodium carbonate (2 M). The precision of Coulter counter
294 measurements of sortable silt mean size ($\overline{\text{SS}}$) is $\pm 1.5\%$ when SS concentrations exceed 5% of
295 the <63 μm fraction (Bianchi et al., 1999; McCave and Hall, 2006). Whereas the $\kappa_{\text{ARM}}/\kappa$
296 magnetic grain-size parameter indicates a progressive fining of magnetite grain size across the
297 Termination (Fig. 9a), the mean sortable-silt parameter indicates no progressive change across
298 the Termination, but rather sortable-silt fining during Heinrich Stadial (HS)-1A followed by
299 relative coarsening in the Bølling-Allerød warm period and then fining in the Younger Dryas
300 (Fig. 9b). The traditional interpretation would be that reduced/increased vigor of bottom
301 currents led to reduced/increased mean sortable-silt grain size during cold and warm intervals,
302 respectively. The increase in $\kappa_{\text{ARM}}/\kappa$ from the Younger Dryas (YD) is due to increases in
303 ARM intensity and susceptibility (κ) at the onset of HS-1A and the subsequent increase and

304 decrease in ARM intensity and susceptibility, respectively, from the end of the Bølling-
305 Allerød warm period (Fig. 9a).

306 The decoupling of the sortable-silt grain size and magnetic grain size parameters (Fig. 9)
307 is due to the fact that magnetic and sortable-silt parameters are sensitive to very different
308 grain-size ranges. The sortable-silt parameter is sensitive to the 10-63 μm grain size (of
309 silicates and silica) and the magnetic parameters are mainly sensitive to the submicron to few
310 micron grains of one mineral (magnetite) that may occur as isolated grains or be incorporated
311 as inclusions in other minerals. Our interpretation is that the sortable-silt parameter is, indeed,
312 a monitor of bottom-current strength and is sensitive to millennial-scale fluctuation in bottom
313 currents across the Termination. The magnetic grain-size parameters, on the other hand, are
314 largely sensitive to grain sizes below the size associated with hydrodynamically sensitive
315 grains that monitor bottom-current velocity.

316 The M_r/M_s ratios, determined from individual hysteresis loops after subtraction of the
317 paramagnetic influence, indicate fining of magnetite grain size at Termination I (Fig. 9c)
318 during the interval of fining indicated by the $\kappa_{\text{ARM}}/\kappa$ parameter (Fig. 9a).

319 Extraction of the FORC central-ridge was performed by masking the central ridge,
320 defined here as the region with $|B_u| < 5 \text{ mT}$ (Fig. 10), and applying locally weighted
321 regression smoothing (Harrison and Feinberg, 2008) to the remaining signal (using smoothing
322 factor 12). The resulting smoothed and extrapolated background (detrital) signal was
323 subtracted from the total FORC distribution to isolate the ridge signal (Fig. 10b). The ridge
324 signal (light green in Fig. 9c) provides a measure of the varying SD concentration. The
325 detrital (background) fraction from the ridge extraction procedure, expressed as
326 $[\text{Detrital}/(\text{SD}+\text{Detrital})]$ (red in Fig. 9c) mimics the M_r/M_s parameter (Fig. 9c).

327 PCA analyses of FORCs demonstrate that the first two principal components describe
328 most (83.5%) of the variability in the FORC data, hence we employed an unmixing model
329 with three end members (EMs) to characterize the system (Fig. 11). One EM comprises the
330 SD fraction (EM2, representative of bacterial magnetosomes), with resulting concentration
331 (dark green in Fig. 9c) that agrees with the results of the ridge extraction method (light green
332 in Fig. 9c). The other two EMs comprise the detrital fraction: EM1 represents the PSD
333 component (~1-5 μm grains) and EM3 represents the MD component (~5-20 μm grains). The
334 concentrations of these detrital fractions are plotted in Figure 9c (black triangles: MD, orange
335 squares: PSD).

336 Quantitative FORC analysis demonstrates that the change in bulk magnetic grain size
337 parameters ($\kappa_{\text{ARM}}/\kappa$ and M_r/M_s) observed over Termination I (Fig. 9) are the result of a
338 change in the relative proportions of two distinct magnetic components, bacterial SD
339 magnetosomes versus detrital (PSD and MD) grains, rather than a decrease in the average
340 grain size of a single magnetite population. The analysis reveals that the change in bulk
341 magnetic grain size parameters is explained entirely by the decreasing concentration of
342 detrital magnetite. The magnetic contribution from SD biogenic magnetosomes (the ridge
343 signal) remains more or less constant in the interval covered by the FORCs (Fig. 9c), based on
344 both the ridge extraction and PCA methods of analysis.

345

346 **7. TEM observations**

347 For transmission electron microscopy (TEM), a magnetic extract from the Holocene of
348 Core MD04-2822 (11-15 cm below seafloor) was prepared by sonicating ~20 cm^3 of sediment
349 in a sodium metaphosphate dispersant. The solution was transferred a reservoir feeding a

350 circulating system driven by a peristaltic pump that allowed the fluid to pass slowly past the
351 outside of a test-tube containing a rare-earth magnet. The material that adhered to the outside
352 of the test-tube was then removed to a methanol solution using a methanol squeeze-bottle.
353 Grains of magnetic separate were encouraged to adhere to a 3 mm copper TEM grid using
354 another magnet suspended a few cm above the TEM grid floating at the surface of the
355 methanol solution. Observations were made using a JEOL JEM-2010F high-resolution (HR)
356 TEM in conjunction with energy dispersive x-ray spectroscopy (EDS) at an accelerating
357 voltage of 200 kV. The microscope is equipped with a Gatan MultiScan Camera Model 794
358 for imaging and an Oxford Instruments detector with INCA 4.05 software for microanalysis.
359 Spot analyses were conducted in STEM mode with a nominally ~1 nm probe size and a
360 camera length of 12 cm.

361 Observation of the Holocene magnetic extract (Fig. 12) indicated grains with shape and
362 size typical for biogenic (bacterial) magnetite (e.g., Vali et al., 1987; Lean and McCave, 1998;
363 Koop and Kirschvink, 2008; Roberts et al., 2011, 2012; Yamazaki, 2012; Channell et al.,
364 2013). Several EDS spectra derived from spots in the center of typically-biogenic individual
365 grains indicate that they contain Fe and O (including Cu from the TEM grid), but no Ti (Fig.
366 12), a magnetite composition typical for bacterial magnetosomes but not for detrital
367 titanomagnetite.

368

369 **8. Discussion**

370 Core MD04-2822 from the Rockall Trough has high sedimentation rate during MIS 2 and
371 Termination I, combined with high-quality age control. The directional magnetic record
372 features an apparent magnetic excursion at ~16 mbsf that occupies about 35 cm of core (Figs.

373 3 and 5). U-channel samples, after AF demagnetization, and cubic 7-cm³ discrete samples,
374 after AF and thermal demagnetization, all indicate the presence of component magnetization
375 directions that have steep negative inclination (Fig. 4), and are close to reverse polarity with
376 virtual geomagnetic poles (VGPs) at high southerly latitudes (Fig. 5). The age model implies
377 an age for the midpoint for the “Rockall” excursion of 26.5 ka and a duration for the
378 excursion of ~350 years (Fig. 5).

379 The Laschamp excursion at ~41 ka is the best documented of all magnetic excursions,
380 and is well known from widely distributed sedimentary deep-sea cores (e.g. Laj et al., 2000;
381 2006; Channell, 2006; Channell et al., 2000; Mazaud et al., 2002; Lund et al., 2005; Channell
382 et al., 2013) and volcanic rocks exposed on land in France (e.g., Laj et al., 2014), and has
383 duration of <1 kyr. Magnetic excursions younger than the Laschamp excursion are
384 controversial. The excursion recorded at Wilson Creek (Mono Lake) was originally referred
385 to as the “Mono Lake excursion” and has usually been assigned an age of ~32 ka based on
386 radiocarbon ages from the Great Basin (Liddicoat and Coe, 1979; Benson et al., 2003; Cassata
387 et al., 2010). In recent years, a body of evidence has accumulated that the excursion recorded
388 at Wilson Creek is, in fact, coeval with the Laschamp excursion (Kent et al., 2002;
389 Zimmerman et al., 2006; Cox et al., 2012; Vazquez and Lidzbarski, 2012) implying the
390 radiocarbon ages from the Mono Lake region are biased by recent contamination. On the
391 other hand, excursions at ~32 ka have been recorded in the North Atlantic (Channell, 2006),
392 in volcanic rocks from New Zealand (Casasta et al., 2008) and Tenerife (Kissel et al., 2011),
393 and in the Great Basin of California outside Wilson Creek (Benson et al., 2013; Negrini et al.,
394 2014). In deep boreholes (SOH1 and SOH4) that recovered several hundred meters of basalt
395 from Hawaii, Teanby et al. (2002) found several intervals where NRM components have

396 negative inclinations, at ~20 ka, ~35 ka and ~40 ka. The K-Ar and Ar/Ar age control has low
397 resolution due to low potassium content of the basalts, and ages are therefore poorly
398 constrained. Teanby et al. (2002) associated the youngest of the three negative-inclination
399 intervals with an anomalously low site-mean inclination (8.5° versus $\sim 35^\circ$) from Hilina Pali,
400 Hawaii (Coe et al., 1978) that had a radiocarbon age of ~18 ka (Rubin and Berthold, 1961).
401 The two older intervals of negative inclination from the SOH1 and SOH4 boreholes (Hawaii)
402 were associated with the Mono Lake excursion and the Laschamp excursion (Teanby et al.,
403 2002). Finally, Zhu et al. (2000) recorded an apparent excursion in a thick flow from the
404 Tianchi Volcano (China) that has been recently dated using $^{40}\text{Ar}/^{39}\text{Ar}$ methods to 17 ka,
405 associated with Hilina Pali, and labeled the Hilina Pali/Tianchi excursion (Singer et al., 2014).
406 The results of this paper add another potential excursion (the “Rockall” excursion at ~26 ka)
407 to the confusing picture of possible post-Laschamp magnetic excursions. The apparent
408 duration of the “Rockall” excursion (~350 years) is such that it is unlikely that it would be
409 recorded at normal pelagic sedimentation rates (<20 cm/kyr) due to the smoothing effects of
410 bioturbation and a finite magnetization lock-in zone below the uppermost bioturbated layer.
411 The high sedimentation rates in the 13-30 ka interval in Core MD04-2822 (Fig. 2), and the
412 uniform silty clay lithology, have apparently facilitated the recording of this putative magnetic
413 excursion.

414 Alternating field and thermal demagnetization of u-channels and discrete samples (Fig.
415 4), other magnetic parameters (Fig. 7), and TEM observations (Fig. 12) indicate that the
416 magnetizations in Cores MD04-2822 are carried by a mixture of detrital (PSD and MD)
417 magnetite and bacterial SD magnetite (magnetosomes). FORC diagrams show a combination
418 of a prominent ridge along the horizontal B_c axis, superimposed on a vertically and

419 horizontally spread background (Fig. 10a). The horizontal ridge (also known as the central
420 ridge) is diagnostic of non-interacting uniaxial SD grains (Newell, 2005; Egli et al., 2010;
421 Harrison and Lascu, 2014), and samples that contain magnetosomes (e.g. Egli et al., 2010;
422 Roberts et al., 2011, 2012; Yamazaki, 2012; Channell et al., 2013). Partly on the basis of
423 TEM observations (Fig. 12), we can associate the central ridge with the presence of
424 magnetosome relics of magnetotactic bacteria, and the background signal with detrital
425 PSD+MD (titano)magnetite. Two methods of analysis of FORC diagrams (ridge extraction
426 and FORC-PCA) over Termination I in Core MD04-2822 indicate that decreasing
427 concentration of the detrital fraction accounts for the bulk magnetic grain-size decrease (as
428 measured by κ_{ARM}/κ and M_r/M_s), and that the SD (magnetosome) fraction is relatively
429 constant over the measured interval (Figs. 9c). The change in magnetic grain size denoted by
430 bulk parameters κ_{ARM}/κ and M_r/M_s immediately post-dates an abrupt six-fold drop in
431 sedimentation rate from ~ 118 cm/kyr to ~ 18 cm/kyr (Fig. 9).

432 Although the κ_{ARM}/κ and M_r/M_s ratios track the detrital signal in the 5-12 ka interval,
433 these ratios fail to reflect the large variations in absolute EM signals that are observed prior to
434 15 ka. FORC-PCA provides a more fundamental tracer of magnetic variations in these
435 sediments than traditional grain size proxies. Ratios such as κ_{ARM}/κ and M_r/M_s can be linked
436 to (and, in principle, entirely derived from) the absolute EM signals identified by FORC-PCA.
437 This principle is illustrated by the excellent agreement between M_r/M_s and the FORC-derived
438 detrital fraction from ridge extraction [Detrital/(SD+Detrital)] (red in Fig. 9c). Examination of
439 the absolute EM signals, however, reveals a more comprehensive picture of the magnetic
440 variations that occur throughout the core, which correlates well with inferred geological
441 processes. The FORC-PCA method indicates a trend within MIS 2 of varying proportions of

442 PSD and MD detrital grains, and within MIS 1 (<11.7 ka) a decreasing trend of the PSD+MD
443 (detrital) fraction (Fig.11). Elevated MD magnetite concentrations during the Bølling-Allerød
444 warm period are consistent with enhanced bottom-current velocity from the mean grain size
445 of sortable silt (Fig. 9c). High PSD+MD magnetite concentration within HS-1A at 16.1 ka
446 (Fig. 9c) coincides with increased concentrations of ice-rafted debris (IRD) associated with
447 H1 (e.g., Scourse et al., 2009). A small peak is observed exclusively in the PSD signal at 12.1
448 ka, which may be associated with the Vedde ash. Prior the Bølling-Allerød warm period,
449 during HS-1A and HS-1B, a slight decrease with age in SD and MD magnetite concentration
450 is accompanied by a more marked decrease in the PSD magnetite concentration.

451

452 **9. Conclusions**

453 An apparent magnetic excursion at ~26.5 ka in Core MD04-2822, with duration of ~350
454 years, was found in u-channel samples, and in discrete samples after both AF and thermal
455 demagnetization. This observation adds to the confusion surrounding magnetic excursions in
456 the 15-30 ka interval, augmenting observations from Hawaii and China for the presence of a
457 magnetic excursion in this interval. The excursion is associated with a minimum in the
458 relative paleointensity (RPI) record (Fig. 6) that can be correlated to a minimum in
459 geomagnetic field intensity derived from cosmogenic isotope fluxes in Greenland ice cores
460 (Muscheler et al., 2005).

461 We demonstrate that FORC-PCA can be used to identify the absolute variations in
462 magnetic contributions from physically identifiable EMs that can be linked to geological
463 processes (e.g., bacterial production/magnetosome dissolution, bottom-current strength,
464 detrital source, and IRD input). Magnetic grain size sensitive parameters and ratios that are

465 often measured (e.g., κ_{ARM}/κ and M_r/M_s) can be entirely derived from the fundamental EM
466 signals, and, it could be argued, become superfluous after FORC-PCA analysis.

467 PCA-FORC analysis indicates that detrital (PSD+MD) magnetite concentrations increase
468 into the Bølling-Allerød warm period and are progressively reduced from the onset of the
469 Younger Dryas (~13 ka) to ~8 ka (Fig. 8), leaving sediment that is increasingly dominated by
470 the relatively constant SD biogenic (magnetosome) signal. We interpret the changes in
471 magnetic parameters as being primarily linked to changes in sources of detritus carried to the
472 site by bottom-currents.

473 From models of glacial rebound in the region, combined with paleodepth data from cores
474 located south of St. Kilda on the Scottish continental shelf west of the Outer Hebrides, water
475 depths began to increase at ~13 ka continuing until ~7 ka, with sea-level rise in this interval of
476 ~70 m (Lambeck, 1995). Contemporaneous with this sea-level rise, deep-water masses in the
477 Rockall Trough likely switched from being dominated by SSW to being dominated by
478 NEADW and LSW (Curry and Oppo, 2005). The decrease in grain size of magnetite from 12
479 ka to 8 ka, and a similar decrease at Termination II, lag benthic $\delta^{18}\text{O}$ and are more
480 synchronous with benthic $\delta^{13}\text{C}$ and XRF ratios (Zr/Sr and Si/Sr) indicative of detrital input
481 (Fig. 8). The timing of magnetite grain size fining (12-8 ka), is interpreted as due to the
482 progressive shutdown of detrital sources linked to contemporaneous sea level rise and to
483 contemporaneous bottom-water reorganization at ~2000 m water depth in the Rockall Trough,
484 as northerly-sourced waters supplanted SSW.

485

486 **Acknowledgements:** Research supported by US NSF grants 0850413 and 1014506, and the
487 European Research Council under the European Union's Seventh Framework Programme

488 (FP/2007-2013) / ERC Grant Agreement No. 320750. The UK NERC and BGS funded the
489 recovery of Core MD04-2822. We thank Kainian Huang for work in the paleomagnetic
490 laboratory at the University of Florida, the Captain and crew of the *Marion Dufresne* for their
491 support during recovery of Core MD04-2822, and Bryan Lougheed and an anonymous
492 reviewer for thorough reviews of the manuscript. Data archived at the Pangaea Database
493 (www.pangaea.de).

494

495 **References**

- 496 Armishaw, J.E., R.W. Holmes, and D.A. Stow, The Barra Fan: a bottom-current reworked,
497 glacially fed submarine fan system. *Marine and Petroleum Geology*, 17, 219-238, 2000.
- 498 Austin, W.E. N., and F.D. Hibbert, Tracing time in the ocean: a brief review of
499 chronological constraints (60-8 kyr) on North Atlantic marine event-based
500 stratigraphies. *Quaternary Science Reviews*, 36, 28-37, 2012.
- 501 Austin, W.E.N., Bard, E., Hunt, J.B., Kroon, D., and J.D. Peacock, The ^{14}C age of the
502 Icelandic Vedde Ash: Implications for Younger Dryas marine reservoir age corrections.
503 *Radiocarbon*, 37(1), 53-62, 1995.
- 504 Banerjee, S.K., J. King and J. Marvin, A rapid method for magnetic granulometry with
505 applications to environmental studies. *Geophysical Res. Lett.*, 8 (4), 333-336, 1981.
- 506 Bazin, L. et al., An optimized multi-proxy, multi-site Antarctic ice and gas orbital
507 chronology (AICC2012): 120-800 ka. *Climate of the Past*, 9(4), 1715-1731,
508 doi:10.5194/cp-9-1715-2013, 2013.
- 509 Benson, L, J. Liddicoat, J. Smoot, A. Sarna-Wojcicki, R. Negrini, and S. Lund, Age of the
510 Mono Lake excursion and associated tephra. *Quaternary Science Reviews*, 22, 135–140,
511 2003.
- 512 Benson, L., J. Smoot, S. Lund, S. Mensing, F. Foit, Jr. and R. Rye, Insights from a synthesis
513 of old and new climate-proxy data from the Pyramid and Winnemucca lake basins for
514 the period 48-11.5 cal ka, *Quat. Inter.*, 310, 62-82, doi:10.1016/j.quaint.2012.02.040,
515 2013.

- 516 Bianchi, G.G., Hall, I.R., McCave, I.N., Joseph, L., Measurement of the sortable silt current
517 speed proxy using the Sedigraph 5100 and Coulter Multisizer II: Precision and
518 accuracy. *Sedimentology* 46, 1001-1014, 1999.
- 519 Bronk Ramsey, C. Deposition models for chronological records. *Quaternary Science*
520 *Reviews* 27, 42-60, 2008.
- 521 Bronk Ramsey, C., Lee, S. Recent and planned development of the program OxCal.
522 *Radiocarbon* 55(2-3), 720-730. 2013.
- 523 Brown, L., G.T. Cook, A.B. MacKenzie, J. Thompson, Radiocarbon age profiles and size
524 dependency of mixing in northeast Atlantic sediments. *Radiocarbon*, 43 (2B), 929-937,
525 2001.
- 526 Cassata, W., Singer, B., Liddicoat, J., Coe, R. Reconciling discrepant chronologies for the
527 geomagnetic excursion in the Mono Basin, California: Insights from new $^{40}\text{Ar}/^{39}\text{Ar}$
528 dating experiments and a revised paleointensity correlation. *Quat. Geochron.* 5, 533-
529 543, 2010.
- 530 Cassata, W., Singer, B., Cassidy, J. Laschamp and Mono Lake excursions recorded in New
531 Zealand. *Earth Plan. Sci. Lett.* 268 76-88, 2008.
- 532 Carter-Stiglitz, B., B. Moskowitz and M. Jackson, Unmixing magnetic assemblages and the
533 magnetic behavior of bimodal mixtures. *J. Geophys. Res.*, 106, 26,397-26, 411, 2001.
- 534 Channell, J.E.T., Late Brunhes polarity excursions (Mono Lake, Laschamp, Iceland Basin
535 and Pringle Falls) recorded at ODP Site 919 (Irminger Basin). *Earth Planet. Sci. Lett.*,
536 244, 378-393, 2006.
- 537 Channell, J.E.T., J.S. Stoner, D.A. Hodell and C.D. Charles. Geomagnetic paleointensity for
538 the last 100 kyr from the subantarctic South Atlantic: a tool for inter-hemispheric

- 539 correlation. *Earth Planet. Sci. Letters*, 175, 145-160, 2000.
- 540 Channell, J.E.T., and Y. Guyodo, The Matuyama Chronozone at ODP Site 982 (Rockall
541 Bank): Evidence for decimeter-scale magnetization lock-in depths, In: “Timescales of
542 the Paleomagnetic Field”. J.E.T. Channell, D.V. Kent, W. Lowrie and J. Meert
543 (editors), AGU Geophysical Monograph 145, 205-219, 2004.
- 544 Channell, J.E.T., C. Xuan, and D.A. Hodell, Stacking paleointensity and oxygen isotope
545 data for the last 1.5 Myrs (PISO-1500). *Earth Planet. Sci. Lett.*, 283, 14-23, 2009.
- 546 Channell, J.E.T., D.A. Hodell and J.H. Curtis, ODP Site 1063 (Bermuda Rise) revisited:
547 oxygen isotopes, excursions and paleointensity in the Brunhes Chron. *Geochem.*
548 *Geophys. Geosyst. (G³)*, 13(1), Q02001, doi:10.1029/2011GC003897, 27 pp., 2012.
- 549 Channell, J.E.T., D.A. Hodell, V. Margari, L.C. Skinner, P.C. Tzedakis, and M.S. Kesler,
550 Biogenic magnetite, detrital hematite, and relative paleointensity in sediments from the
551 Southwest Iberian Margin, *Earth Planet. Sci. Letters*, 376, 99-109, 2013.
- 552 Coe, R.S., S. Grommé and E.A. Mankinen, Geomagnetic paleointensities from radiocarbon-
553 dated lava flows on Hawaii and the question of the Pacific non-dipole low. *J. Geophys.*
554 *Res.*, 83, 1740-1756, 1978.
- 555 Cox, S.E., K.A. Farley, and S.R. Hemming, Insights into the age of the Mono Lake
556 Excursion and magmatic crystal residence time from (U-Th)/He and Th-230 dating of
557 volcanic allanite. *Earth and Planetary Science Letters* 319, 178-184, 2012.
- 558 Croudace, I.W., A. Rindby and R.G. Rothwell, ITRAX: description and evaluation of a new
559 multi-function X-ray core scanner. In : Rothwell, R.G. (Editor), *New techniques in*
560 *sediment core analysis*. Geol. Soc. London, Spec. Pub., 267, 51-63, 0305-
561 8719/06/\$15.00, Geological Society of London, 2006.

- 562 Curry W.B., and D.W. Oppo, Glacial water mass geometry and the distribution of $\delta^{13}\text{C}$ of
563 ΣCO_2 in the western Atlantic Ocean. *Paleoceanography* 20, PA1017, 2005.
- 564 Day, R., M. Fuller, and V.A. Schmidt, Hysteresis properties of titanomagnetites: grain-size
565 and compositional dependence. *Phys. Earth Planet. Int.*, 13, 260-267, 1977.
- 566 Dunlop, D.J., Theory and application of the Day plot (M_{rs}/M_s versus H_{cr}/H_c) 1. Theoretical
567 curves and tests using titanomagnetite data. *J. Geophys. Res.*, 107, B3, 2056,
568 doi:10.1029/2001JB000486, 2002.
- 569 Dunlop, D.J. and B. Carter-Stiglitz, Day plots of mixtures of superparamagnetic, single
570 domain, pseudosingle domain, and multidomain magnetites. *J. Geophys. Res.*, 111,
571 B12S09, doi: 10.1029/2006JB004499, 2006.
- 572 Egli, R., VARIFORC: An optimized protocol for calculating non-regular first-order reversal
573 curve (FORC) diagrams, *Glob. Planet. Change*, 110(PC), 302–320,
574 doi:10.1016/j.gloplacha.2013.08.003, 2013.
- 575 Egli, R., A. P. Chen, M. Winklhofer, K. P. Kodama and C-S. Horng, Detection of
576 noninteracting single domain particles using first-order reversal curve diagrams.
577 *Geochemistry, Geophysics, Geosystems*, 11 (1), Q01Z11, doi:10.1029/2009GC002916,
578 2010.
- 579 Guyodo, Y., J.E.T. Channell and R. Thomas, Deconvolution of u-channel paleomagnetic
580 data near geomagnetic reversals and short events. *Geophys. Res. Letters*, 29, 1845,
581 doi:10.1029/2002GL014963, 2002.
- 582 Harkness, D.D, The extent of the natural ^{14}C deficiency in the coastal environment of the
583 United Kingdom, *Journal of the European Study Group on Physical, Chemical and*
584 *Mathematical Techniques Applied to Archaeology PACT* 8 (IV.9), 351-364, 1983.

- 585 Harrison, R. J., and I. Lascu, FORCulator: A micromagnetic tool for simulating first-order
586 reversal curve diagrams, *Geochemistry Geophys. Geosystems*, 15, 4671–4691,
587 doi:10.1002/2014GC005582, 2014.
- 588 Harrison, R.J. and J.M. Feinberg, FORCinel: An improved algorithm for calculating first-
589 order reversal curve distributions using locally weighted regression smoothing.
590 *Geochem., Geophysics, Geosystems.*, 9, Q05016, doi:10.1029/2008GC001987, 2008.
- 591 Håkansson, S, University of Lund Radiocarbon Dates III. *Radiocarbon* 12: 534-552. 1970.
- 592 Heslop, D., On the statistical analysis of the rock magnetic S-ratio. *Geophys. J. Int.*, 178,
593 159-161, 2009.
- 594 Hibbert, F.D., W.E.N. Austin, M.J. Leng and R.W. Gatliff, British ice sheet dynamics
595 inferred from North Atlantic ice-rafted debris records spanning the last 17 500 years. *J.*
596 *Quaternary Sci.*, 25, 461-482, 2010.
- 597 Hibbert, F.D., S. Wastegard, R. Gwynn and W.E.N. Austin, Identification of a MIS 6 age (c.
598 180 ka) Icelandic tephra within NE Atlantic sediments: a new potential
599 chronostratigraphic marker. In: Austin, W. E. N., Abbott, P. M., Davies, S. M., Pearce,
600 N. J. G. and Wastegard, S. (eds) *Marine Tephrochronology*. Geological Society,
601 London, Special Publications, 398, 65-80, 2014. <http://dx.doi.org/10.1144/SP398.10>.
- 602 Kent D.V., S.R. Hemming, and B.D. Turrin, Laschamp excursion at Mono Lake? *Earth and*
603 *Planetary Science Letters* 197: 151–164, 2002.
- 604 King, J.W., S.K. Banerjee, and J. Marvin, A new rock-magnetic approach to selecting
605 sediments for geomagnetic paleointensity studies: application to paleointensity for the
606 last 4000 years. *J. Geophys. Res.*, 88, 5911-5921, 1983.

- 607 Kirschvink, J.L., The least squares lines and plane analysis of paleomagnetic data. *Geophys.*
608 *J.R. Astr. Soc.* 62, 699-718, 1980.
- 609 Kissel C., C. Laj, L. Labeyrie, T. Dokken, A. Voelker, and D. Blamart, Rapid climatic
610 variations during marine isotopic stage 3: Magnetic analysis of sediments from Nordic
611 seas and north Atlantic. *Earth and Planet. Sci. Letters* 171, 489–502, 1999.
- 612 Kissel, C., C. Laj, T. Mulder, C. Wandres and M. Cremer, The magnetic fraction : A tracer
613 of deep water circulation in the North Atlantic. *Earth Planet. Sci. Letters*, 288, 444-454,
614 2009.
- 615 Kissel C., H. Guillou, C. Laj, J.C. Carracedo, S. Nomade, F. Perez-Torrado, C. Wandres,
616 The Mono Lake excursion recorded in phonolitic lavas from Tenerife (Canary Islands):
617 paleomagnetic analyses and coupled K/Ar and Ar/Ar dating. *Phys. Earth Planet. Int.*,
618 187, 232-244, doi:10.1016/j.pepi.2011.04.014, 2011.
- 619 Kissel, C., A. Van Toer, C. Laj, E. Cortijo and E. Michel, Variations in strength of the North
620 Atlantic bottom water during the Holocene. *Earth Planet. Sci. Letters*, 369-370, 248-
621 259, 2013.
- 622 Knutz, P.C., W.E.N. Austin and E.J.W. Jones, Millennial-scale depositional cycles related to
623 British Ice Sheet variability and North Atlantic paleocirculation since 45 kyr B.P., Barra
624 Fan, U.K. margin. *Paleoceanography*, 16, 53-64, 2001.
- 625 Knutz, P.C., E.J.W. Jones, W.E.N. Austin and T.C.E. van Weering, Glacimarine slope
626 sedimentation, contourite drifts and bottom current pathways on the Barra Fan, UK
627 North Atlantic margin. *Mar. Geol.* 188, 129–146, 2002.
- 628 Kopp, R.E. and J.L. Kirschvink, The identification and biogeochemical interpretation of
629 fossil magnetotactic bacteria. *Earth Science Reviews*, 86, 42-61, 2008.

- 630 Laj, C. and J.E.T. Channell. Geomagnetic excursions. In: *Treatise on Geophysics: Volume 5,*
631 *Geomagnetism* (editor: M. Kono). Chapter 10, 373-416, Elsevier, Amsterdam, 2007.
- 632 Laj, C., C. Kissel, A. Mazaud, J.E.T. Channell, and J. Beer, North Atlantic paleointensity
633 stack since 75 ka (NAPIS-75) and the duration of the Laschamp event. *Phil. Trans.*
634 *Royal Soc. London*, 358, 1009-1025, 2000.
- 635 Laj, C., C. Kissel, and A. P. Roberts, Geomagnetic field behavior during the Icelandic Basin
636 and Laschamp geomagnetic excursions: a simple transitional field geometry?,
637 *Geochem. Geophys. Geosyst.*, 7, Q03004, doi :10.1029/2005GC001122, 2006.
- 638 Laj, C., H. Guillou and C. Kissel, Dynamics of the Earth's magnetic field in the 10-75 kyr
639 period comprising the Laschamp and Mono Lake excursions: New results from the
640 French Chaîne des Puys in a global perspective. *Earth Planet. Sci. Letters*, 387, 184-
641 197, 2014.
- 642 Lambeck, K., Glacial isostasy and water depths in the late Devensian and Holocene on the
643 Scottish Shelf west of the Outer Hebrides. *J. Quaternary Science*, 10 (1), 83-86, 1995.
- 644 Lascu, I., R. J. Harrison, Y. Li, J. R. Muraszko, J. E.T. Channell, A. M. Piotrowski, and D.
645 A. Hodell, Magnetic unmixing of first-order reversal curve diagrams using principal
646 component analysis. *Geochem. Geophys. Geosyst.*, 16, doi:10.1002/2015GC005909,
647 2015.
- 648 Lean, C.M.B., and I.N. McCave, Glacial to interglacial mineral magnetic and
649 paleoceanographic changes at Chatham Rise, SW Pacific. *Earth Planet. Sci. Letters*,
650 163, 247-260, 1998.
- 651 Liddicoat J.C and R.S. Coe, Mono Lake geomagnetic excursion. *J. Geophys. Res.*, 84: 261-
652 271, 1979.

- 653 Lisiecki, L.E., and M.E. Raymo, A Pliocene-Pleistocene stack of 57 globally distributed
654 benthic $d^{18}O$ records. *Paleoceanography*, 20, PA1003, doi:10.1029/2004PA001071,
655 2005.
- 656 Lowrie, W., Identification of ferromagnetic minerals in a rock by coercivity and unblocking
657 temperature properties. *Geophys. Res. Letters*, 17, 159-162, 1990.
- 658 Lund, S.P., M. Schwartz, L. Keigwin, and T. Johnson, Deep-sea sediment records of the
659 Laschamp geomagnetic field excursion (<41,000 calendar years before present). *J.*
660 *Geophys. Res.*, 110, Q12006, doi :10.1029, 2005GC001036, 2005.
- 661 Mazaud, A., M.A. Sicre, U. Ezat, J.J. Pichon, J. Duprat, C. Laj, C. Kissel, L. Beaufort, E.
662 Michel, and J.L. Turon, Geomagnetic-assisted stratigraphy and sea surface temperature
663 changes in core MD94-103 (Southern Indian Ocean): possible implications for North-
664 South climatic relationships around H4. *Earth Planet. Sci. Lett.*, 201, 159-170, 2002.
- 665 McCave I.N., and I.R. Hall, Size sorting in marine muds: Processes, pitfalls and prospects
666 for palaeoflow-speed proxies. *Geochem. Geophys. Geosyst.* 7, Q10N05,
667 doi:10.1029/2006GC001284, 37 pp., 2006.
- 668 McCave, I.N., B. Manighetti, and S.G. Robinson, Sortable silt and fine sediment
669 size/composition slicing: parameters for palaeocurrent speed and palaeoceanography.
670 *Paleoceanography* 10, 593-610, 1995.
- 671 Muscheler, R., J. Beer, P.W. Kubik and H.-A. Synal, Geomagnetic field intensity during the
672 last 60,000 years based on ^{10}Be and ^{36}Cl from the summit ice cores and ^{14}C . *Quaternary*
673 *Science Reviews*, 24, 1849-1860, 2005.

- 674 Muxworthy, A.R. and A.P. Roberts, First-order reversal curve (FORC) diagrams. In
675 Encyclopedia of Geomagnetism and Paleomagnetism. D. Gubbins and E. Herrero-
676 Bervera (eds.), 266-272, Springer, Dordrecht, Netherlands, 2007.
- 677 Negrini, R.M., D. T. McCuan, W. S. Cassata, J. E. T. Channell, K. L. Verosub, J. R. Knott,
678 R. S. Coe, J.C. Liddicoat, S. P. Lund, R.A. Horton, J. D. Lopez, L. V. Benson, A.M.
679 Sarna-Wojcicki, Nongeocentric axial dipole field behavior during the Mono Lake
680 excursion. *J. Geophys. Res.*, 119, doi:10.1002/2013JB010846, 2014.
- 681 New, A., and D. Smythe-Wright, Aspects of the circulation in the Rockall Trough. *Cont.*
682 *Shelf Res.* 21, 777–810, 2001.
- 683 Newell, A. J., A high-precision model of first-order reversal curve (FORC) functions for
684 single-domain ferromagnets with uniaxial anisotropy, *Geochem., Geophys. Geosyst.*,
685 6(5), Q05010, doi:10.1029/2004GC000877, 2015.
- 686 Olsson, I U, Uppsala natural radiocarbon measurements II. *Am Jour Sci Radiocarbon Supp*
687 2:112-128. 1960.
- 688 Pike, C.R., A.P. Roberts and K.L. Verosub, Characterizing interactions in fine magnetic
689 particle systems using first order reversal curves. *J. Appl. Phys.*, 85, 6660-6667,
690 doi:10.1063/1.370176, 1999.
- 691 Rasmussen S., et al., 2014. A stratigraphic framework for abrupt climatic changes during the
692 Last Glacial period based on three synchronized Greenland ice-core records: Refining
693 and extending the INTIMATE event stratigraphy. *Quaternary Sci. Reviews*, 106, 14-28,
694 2014.

- 695 Roberts, A.P., C.R. Pike, and K.L. Verosub, First-order reversal curve diagrams: A new tool
696 for characterizing the magnetic properties of natural samples. *J. Geophys. Res.*, 105,
697 28,461-28,475, doi:10.1029/2000JB900326, 2000.
- 698 Roberts, A.P and M. Winklhofer, Why are geomagnetic excursions not always recorded in
699 sediments? Constraints from post-depositional remanent magnetization lock-in
700 modeling. *Earth Planet. Sci. letters*, 227, 334-359, 2004.
- 701 Roberts, A.P, F. Florindo, G. Villa, L. Chang, L. Jovane, S.M. Bohaty, J.C. Larrasoana, D.
702 Heslop, J.D. Fitz Gerald, Magnetotactic bacterial abundance in pelagic marine
703 environments is limited by organic carbon flux and availability of dissolved iron. *Earth
704 and Planet. Sci. Letters*, 310, 441-452, 2011.
- 705 Roberts, A.P., L. Chiang, D. Heslop, F. Florindo and J.C. Larrasoana, Searching for single
706 domain magnetite in the “pseudo-single-domain” sedimentary haystack: Implications of
707 biogenic magnetite preservation for sediment magnetism and relative paleointensity
708 determinations. *J. Geophysical Res.*, 117, B08104, doi:10.1029/2012JB009412, 2012.
- 709 Rubin, M. and S.M. Berthold, U.S. Geological Survey radiocarbon dates, VI. *Radiocarbon*,
710 3, 86-98, 1961.
- 711 Scourse, J.D., A.I. Haapaniemi, E. Colmenero-Hidalgo, V.L. Peck, I.R. Hall, W.E.N.
712 Austin, P.C. Knutz and R. Zahn, Growth, dynamics and deglaciation of the last British-
713 Irish ice sheet: the deep-sea ice-rafted detritus record. *Quat. Sci. Revs.*, 28, 3066-3084,
714 2009.
- 715 Singer, B. S., B. R. Jicha, H. He, and R. Zhu, Geomagnetic field excursion recorded 17 ka at
716 Tianchi Volcano, China: New $^{40}\text{Ar}/^{39}\text{Ar}$ age and significance, *Geophys. Res. Lett.*, 41,
717 2794–2802, doi:10.1002/2014GL059439, 2014.

- 718 Skinner, L.C., and I.N. McCave, Analysis and modeling of gravity and piston coring based
719 on soil mechanics. *Marine Geology*, 199, 181-204, 2003.
- 720 Snowball, I., and M. Moros, Saw-tooth pattern of North Atlantic current speed during
721 Dansgaard-Oeschger cycles revealed by the magnetic grain size of Reykjanes Ridge
722 sediments at 59°N. *Paleoceanography*, 18, 1026, doi:10.1029/2001PA000732, 2003.
- 723 Stoker, M.S., The influence of glacial sedimentation on slope-apron development on the
724 continental margin of Northwest Britain. In: *The Tectonics, Sedimentation and
725 Paleoclimatology of the North Atlantic Region*, edited by R.A. Scrutton et al., *Geol.
726 Soc. Spec. Publ.*, 159-177, 1995.
- 727 Stoner, J.S., J.E.T. Channell, A. Mazaud, S.E. Strano and C. Xuan. The influence of high
728 latitude flux lobes on the Holocene paleomagnetic record of IODP Site U1305 and the
729 northern North Atlantic. *Geochem. Geophys. Geosyst.*, 14 (10), doi:
730 10.1002/ggge.20272, 2013.
- 731 Szérmétya, N., F. Bassinot, Y. Balut, L. Labeyrie and M. Pagel, Oversampling of
732 sedimentary series collected by giant piston corer: Evidence and corrections based on
733 3.5-kHz chirp profiles. *Paleoceanography*, 19, PA1005, doi:10.1029/2002PA000795,
734 2004.
- 735 Teanby, N., C. Laj, D. Gubbins and M. Pringle, A detailed paleointensity and inclination
736 record from drill core SOH1 on Hawaii. *Phys. Earth Planet. Int.*, 131, 101-140, 2002.
- 737 Thomas, R., Y. Guyodo and J.E.T. Channell, U-channel track for susceptibility
738 measurements. *Geochemistry, Geophysics and Geosystems (G³)*, 1050, doi:
739 10.1029/2002GC000454, 2003.
- 740 Vali, H., O. Forster, G. Amarantidis and N. Petersen, Magnetotactic bacteria and their

- 741 magnetofossils in sediments. *Earth and Planet. Sci. Letters*, 86, 389-400, 1987.
- 742 Vazquez J.A., and M.I Lidzbarski, High-resolution tephrochronology of the Wilson Creek
743 Formation (Mono Lake, California) and Laschamp event using U-238-Th-230 SIMS
744 dating of accessory mineral rims. *Earth and Planetary Science Letters*, 357, 54-67, doi :
745 10.1016/j.epsl.2012.09.013, 2012.
- 746 Waelbroeck, C., Duplessy, J.C., Michel, E., Labeyrie, L., Paillard, D. and Duprat, J., The
747 timing of the last deglaciation in North Atlantic climate records. *Nature*, 412(6848),
748 pp.724-727, 2001.
- 749 Weeks, R., C. Laj, L. Endignoux, M. Fuller, A. Roberts, R. Manganne, E. Blanchard, and
750 W. Goree, Improvements in long-core measurement techniques: applications in
751 palaeomagnetism and palaeoceanography. *Geophys. J. Int.*, 114, 651-662, 1993.
- 752 Xuan, C. and J.E.T. Channell, UPmag: MATLAB software for viewing and processing u-
753 channel or other pass-through paleomagnetic data. *Geochem. Geophys. Geosyst.*, 10,
754 Q10Y07, doi:1029/2009GC002584, 2009.
- 755 Yamazaki, T., Paleoposition of the intertropical convergence zone in the eastern Pacific
756 inferred from glacial-interglacial changes in terigenous and biogenic magnetic mineral
757 fractions. *Geology*, 40, 151-154, 2012.
- 758 Zhu, R., Y. Pan, and R. S. Coe, Paleointensity studies of a lava succession from Jilin
759 Province, northeastern China: Evidence for the Blake event, *J. Geophys. Res.*, 105,
760 8305–8317, doi:10.1029/1999JB900448, 2000.
- 761 Zimmerman, S. H., S.R. Hemming, D.V. Kent, S.Y. Searle, Revised chronology for late
762 Pleistocene Mono Lake sediments based on paleointensity correlation to the global
763 reference curve. *Earth Planet. Sci. Lett.*, 252, 94-106, 2006.
- 764

765 **Figure captions**

766 Fig. 1. Location of Core MD04-2822 in the Rockall Trough. Modern deep-water flow
 767 comprises NE Atlantic Deep Water (NEADW), Labrador Sea Water (LSW) and Wyville-
 768 Thomson Ridge (at 60° N) Overflow Water (WTOW) (figure modified after Knutz et al.,
 769 2002).

770

771 Fig. 2. Core MD04-2822: (a) Benthic oxygen isotope record (red) compared to the LR04
 772 $\delta^{18}\text{O}$ stack (blue, Lisiecki and Raymo, 2005), (b) Percent *N. pachyderma* (sin.) (green)
 773 compared to the NGRIP Greenland oxygen isotope record with 10 point smoothing (black) for
 774 the last 115 kyr on the GICC05 timescale (Rasmussen et al., 2014 and references therein), and
 775 beyond 120 ka, to the Antarctic (EDC) methane record (dashed brown) on the AICC2012
 776 chronology (Bazin et al., 2013). (c) Inferred sedimentation rates. Colored triangles indicate
 777 sources of age control: radiocarbon (orange), tephra (black), correlation of benthic oxygen
 778 isotope data to the LR04 $\delta^{18}\text{O}$ stack (red), and correlation of percent *N. pachyderma* (sin.) to
 779 NGRIP $\delta^{18}\text{O}$ and to Antarctic (EDC) methane (green).

780 Fig. 3. Component declination, inclination and maximum angular deviation (MAD) values
 781 computed for the 20-80 mT demagnetization interval plotted versus depth (meters below
 782 seafloor, mbsf). Dark blue (light blue) symbols indicate directions associated with MAD
 783 values $<5^\circ$ ($>5^\circ$).

784

785 Fig. 4. Orthogonal projections of demagnetization data in the vicinity of the possible magnetic
 786 excursion: (a-d) u-channel samples during alternating field demagnetization for peak fields of
 787 10-80 mT, (e-f) 7-cm³ discrete sample data after alternating field demagnetization for peak

788 fields of 0-100 mT , (g-j) 7-cm³ discrete sample data after thermal demagnetization for
 789 temperatures of 0-600°C. Red (blue) lines/symbols represent projection on the vertical
 790 (horizontal) plane. Depths below seafloor (cm) in Core MD04-2822 are given (see Fig. 5 for
 791 stratigraphic sequence). Axes are scaled in mA/m.

792

793 Fig. 5. Core MD04-2822: (a) Component declination and inclination from u-channel samples
 794 after alternating field (AF) demagnetization (dots/circles with lines), discrete samples after
 795 AF demagnetization (squares) and thermal demagnetization (triangles) plotted versus depth.
 796 (b) Maximum angular deviation (MAD) values associated with the component directions for
 797 AF demagnetization of u-channel samples (black dots), AF demagnetization of discrete
 798 samples (green squares) and thermal demagnetization of discrete samples (green triangles).
 799 (c) Virtual geomagnetic polar (VGP) latitudes versus age for u-channel samples (black dots),
 800 alternating field demagnetization of discrete samples (green squares) and thermal
 801 demagnetization of discrete samples (red triangles). Location of section break indicated. Map
 802 projection inset: Virtual geomagnetic poles (VGPs) during the ~26 ka magnetic excursion,
 803 indicating three VGP loops leading to VGPs at high southern latitudes during Loop 3
 804 followed by return of VGPs to high northern latitudes.

805

806 Fig. 6. Core MD04-2822: (a) Slopes of NRM/ARM (dark blue), NRM/ARMAQ (light blue)
 807 and NRM/IRM (red) constituting three relative paleointensity (RPI) proxies. (b) The
 808 NRM/ARM RPI proxy (red) compared with RPI proxy determined from the flux of ¹⁰Be (dark
 809 green) and ³⁶Cl (light green) in Greenland ice cores from Muscheler et al. (2005). Yellow

810 shading indicates three RPI minima in Core MD04-2822 corresponding to 26.5, 34.5 and 40.8
 811 ka.

812 Fig. 7. Core MD04-2822: (a) Plot of anhysteretic susceptibility (κ_{ARM}) against susceptibility
 813 (κ) (blue dots) with the calibration of magnetite grain size from King et al. (1983). (b)
 814 Hysteresis ratio plot after Day et al. (1977), with top section (0-150 cm) in light blue, Section
 815 2 (150-300 cm or 8.1-13.0 ka) in purple, and below Section 2 in dark blue. Black triangles:
 816 magnetite grain-size mixing line between the single domain (SD) and multidomain (MD)
 817 fields. Red squares: hysteresis ratios from crushed, sized (unannealed) natural titanomagnetite
 818 (Dunlop, 2002). (c) FORC diagram for sample from 1632 cm below seafloor in the magnetic
 819 excursion interval (see Fig. 5). (d) Thermal demagnetization of a 3-axis IRM applied to 40
 820 samples using orthogonal magnetizing fields of 0.1 T (red), 0.3 T (blue) and 1.2 T (green).

821

822 Fig. 8. Core MD04-2822: (a) $\kappa_{\text{ARM}}/\kappa$ magnetic grain size proxy (red) and benthic $\delta^{18}\text{O}$ (blue)
 823 (b) $\kappa_{\text{ARM}}/\kappa$ (red) and benthic $\delta^{13}\text{C}$ (blue), (c) Zr/Sr (black) and Si/Sr (brown) from X-ray
 824 fluorescence (XRF) core scanning.

825

826 Fig. 9. Core MD04-2822 Termination I: (a) The $\kappa_{\text{ARM}}/\kappa$ (black), volume susceptibility (red
 827 dashed) and ARM intensity (blue dashed) compared with benthic $\delta^{18}\text{O}$ (light green dashed
 828 line) and sedimentation rate changes (green) from ~ 118 cm/kyr at 21 ka to ~ 18 cm/kyr in the
 829 late Holocene. (b) Mean grain-size of sortable silt (blue) and after 5-point smoothing (red). (c)
 830 The saturation remanence over saturation magnetization ratio (M_r/M_s , blue) compared with
 831 results from FORC analysis using the ridge extraction method: single domain (SD) ridge

832 signal (light green) and background (detrital) fraction expressed as Detrital/(SD+Detrital) (red
 833 line). Concentration of end-members (EMs) using FORC principal component analysis
 834 (FORC-PCA): SD (EM2: dark green), PSD (EM1: orange squares), MD (EM3: black
 835 triangles). The 8.2 Event, Younger Dryas (YD), Bølling-Allerød (B-A), Heinrich stadials HS-
 836 1A and HS-1B, and last glacial maximum (LGM) are marked.

837

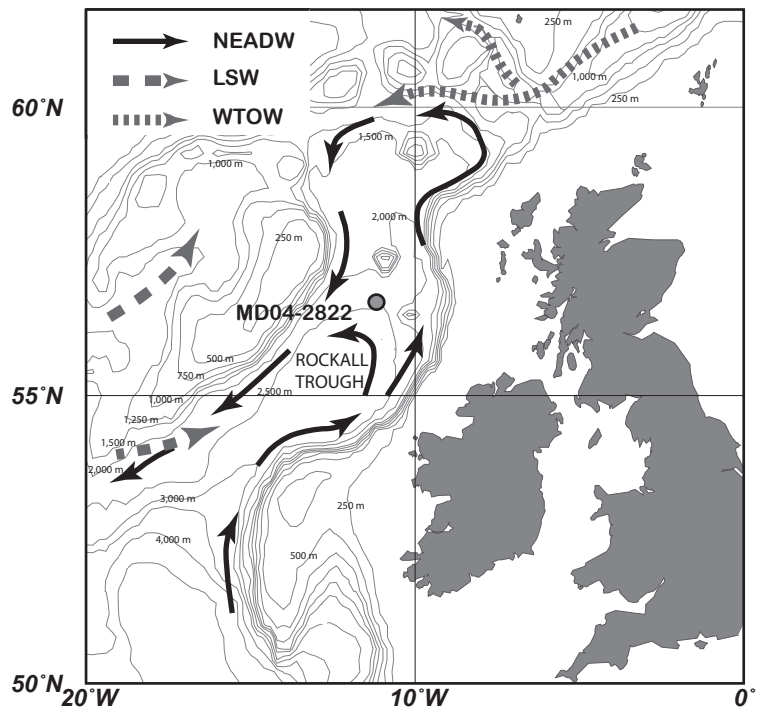
838 Fig. 10. (a) FORC diagrams from 150 cm below seafloor (8.1 ka) and 298 cm below seafloor
 839 (13.0 ka) as end members of the decrease in the detrital magnetite fraction in the 13-8 ka
 840 interval. (b) Smoothed background signal obtained by applying locally weighted regression
 841 smoothing (SF = 12) to data outside the central ridge ($|B_u| < 5$ mT). Central-ridge extraction,
 842 applied to FORC sample at 13.0 ka, by subtracting smoothed background from total FORC
 843 distribution. (c) Profiles along B_u axis at $B_c = 80$ mT (indicated by dashed vertical line in b)
 844 for total (red), smoothed background (dashed) and extracted ridge (black) distributions.
 845 Profiles along B_c axis at $B_u = 0$ mT (indicated by dashed vertical line in b) for total (red),
 846 smoothed background (dashed) and extracted ridge (black) distributions.

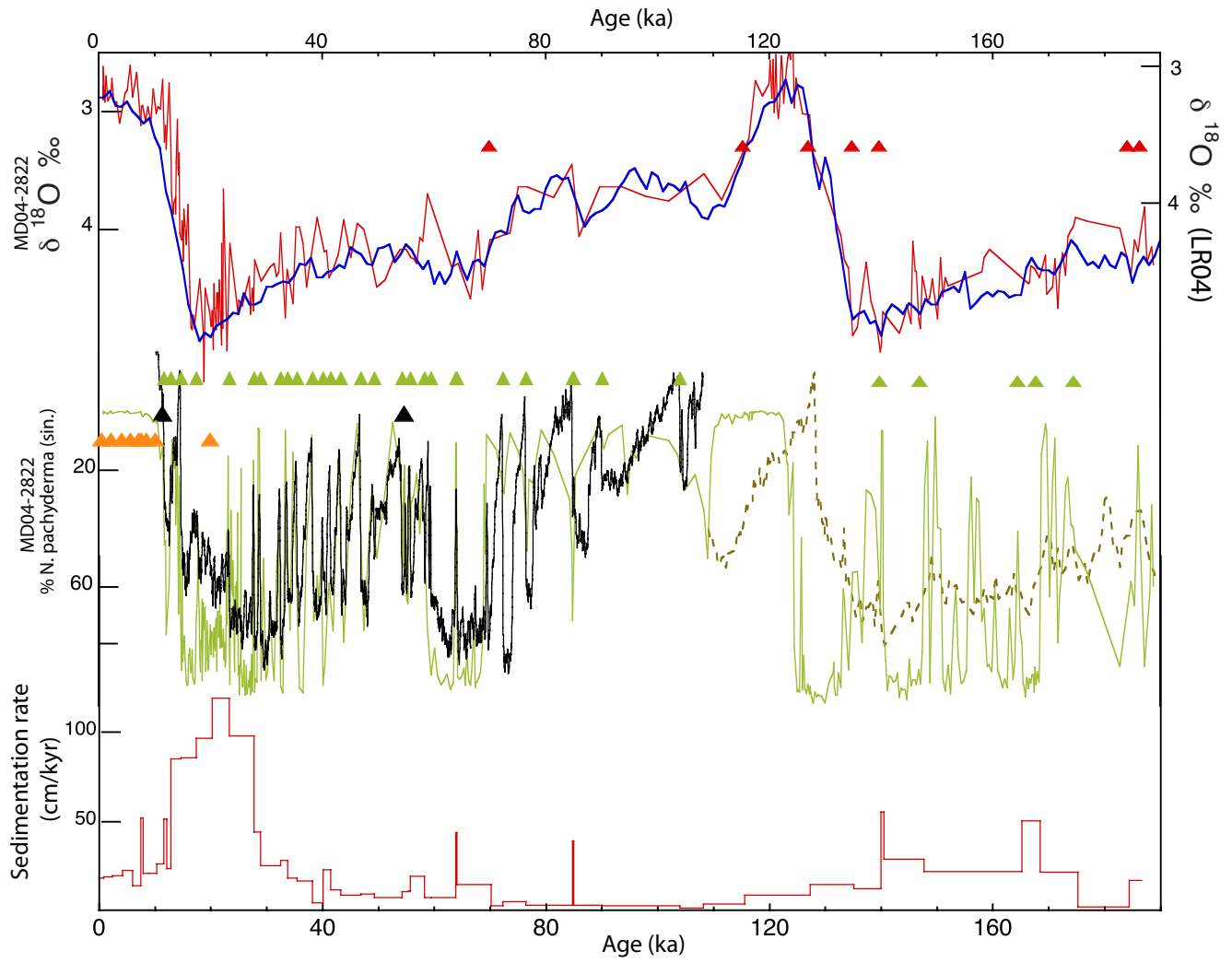
847

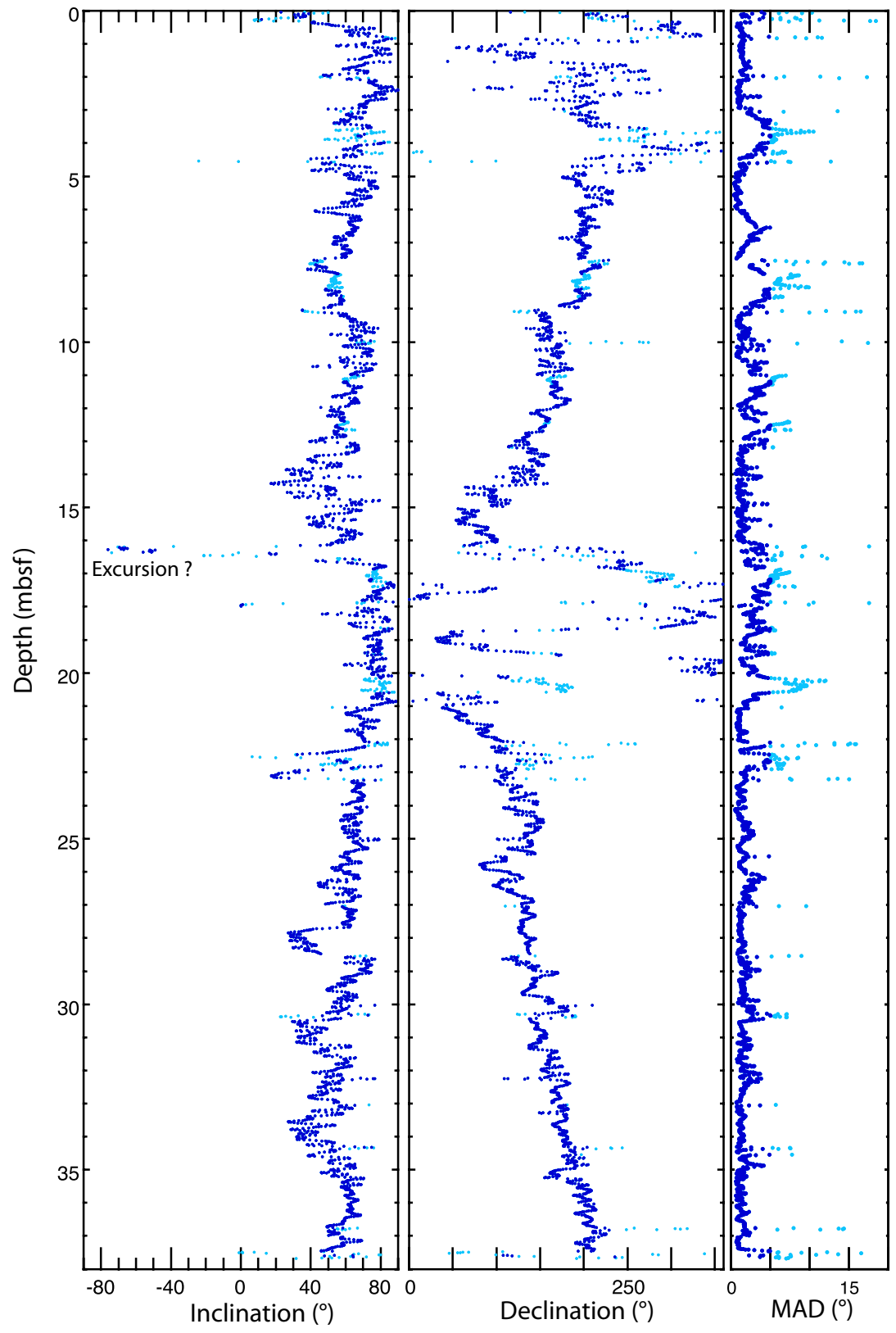
848 Fig. 11. Principal component analysis (PCA) and unmixing model for samples from the 4.5-
 849 18.5 ka interval in Core MD04-2822. a) PCA score plot and unmixing model boundary (red
 850 triangle). Vertices represent end members (EMs). b) Ternary diagram showing relative
 851 abundances of the three EMs. c) Computed FORC diagrams for EM1 (PSD magnetite), EM2
 852 (SD magnetite), and EM3 (MD magnetite). Red and blue symbols in (a) and (b) represent
 853 Holocene (MIS 1, <11.7 ka), and Late Pleistocene (MIS 2, >11.7 ka) samples, respectively.

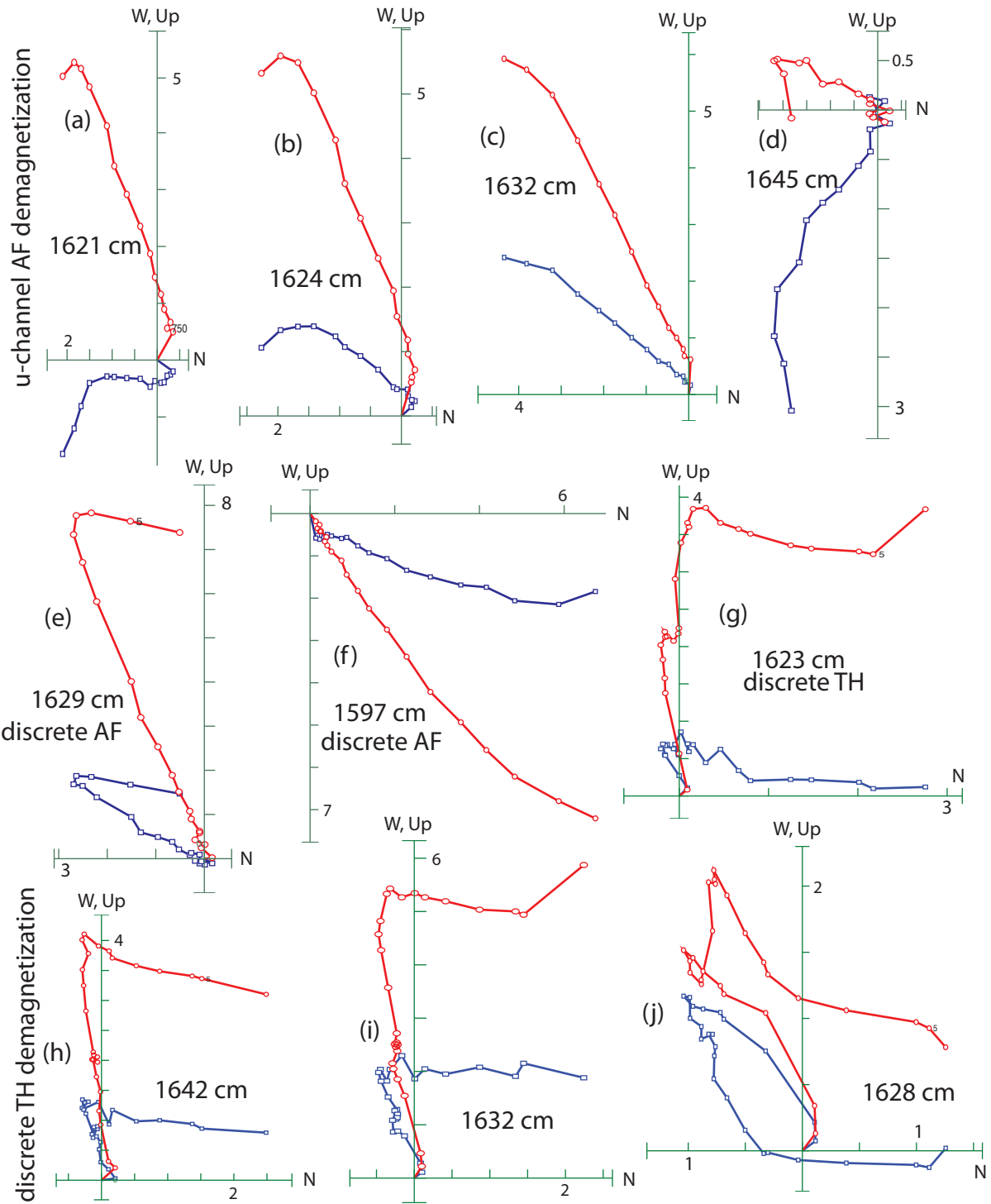
854

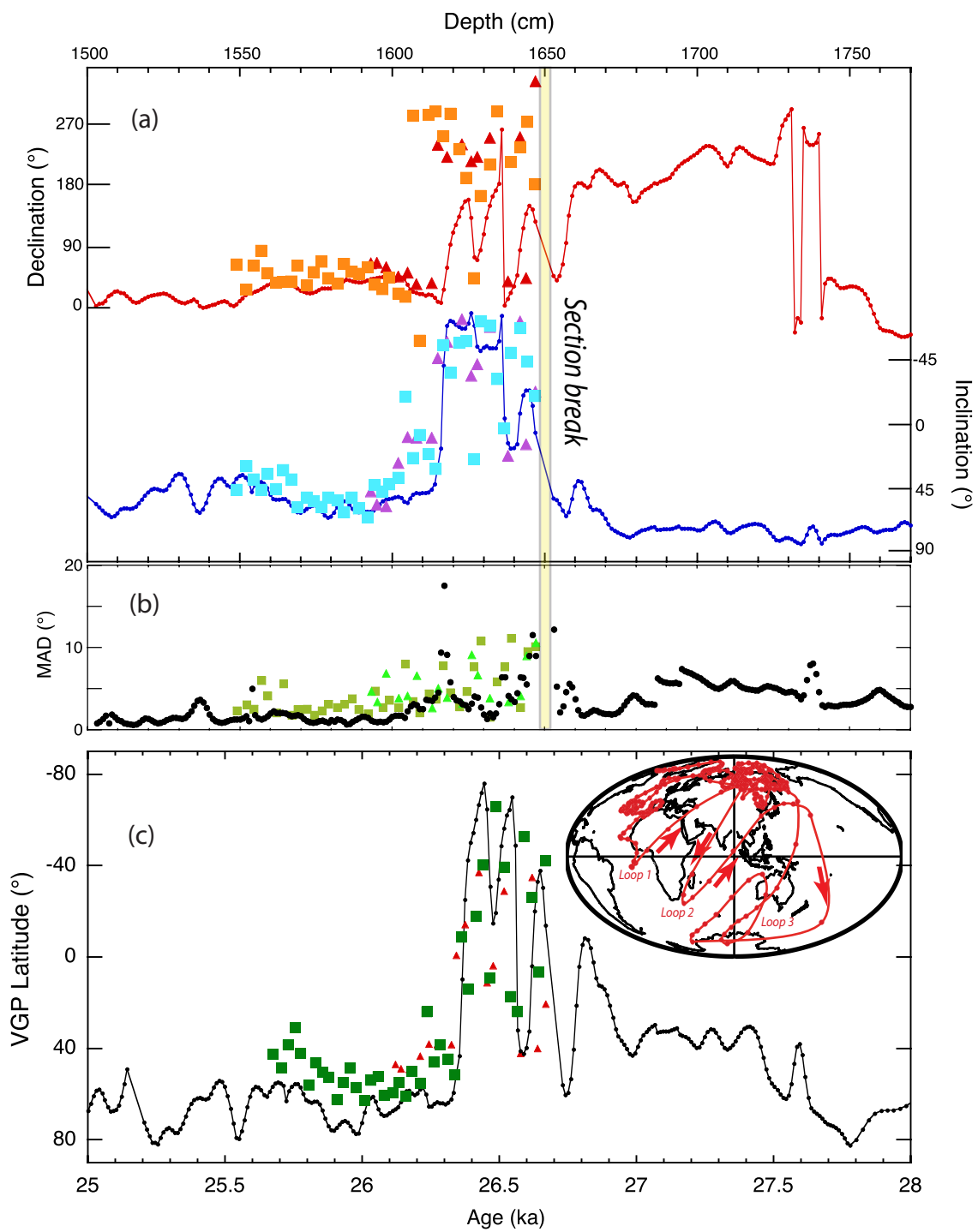
855 Fig. 12. Photomicrographs from transmission electron microscopy (TEM) of a magnetic
856 extract from the Holocene of Core MD04-2822 (11-15 cm below seafloor). Energy-
857 dispersive x-ray spectroscopy (EDS) spectra for (red) spots at the center of two bacterial
858 magnetosomes indicate Fe and O (including Cu from the TEM grid), but no Ti.
859
860

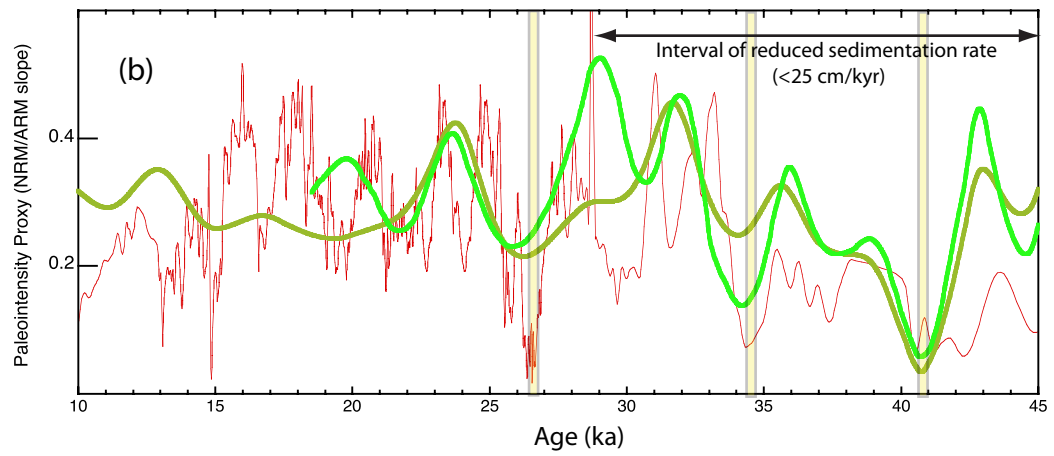
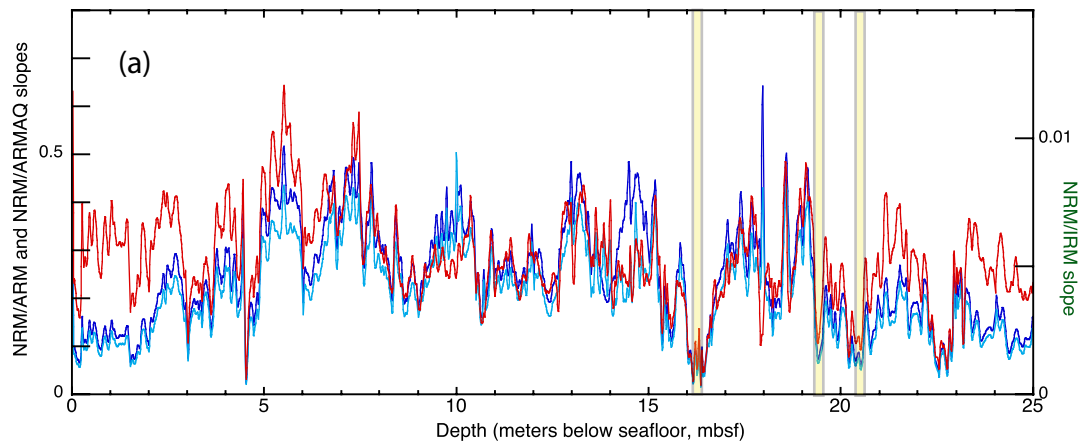


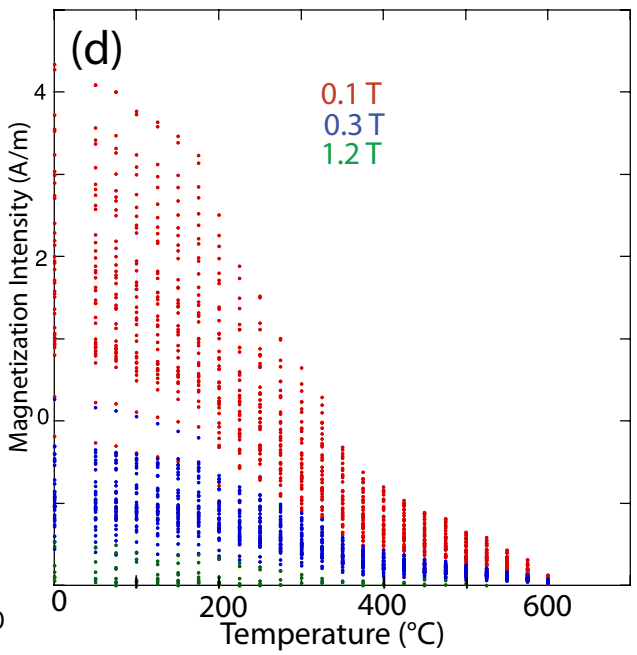
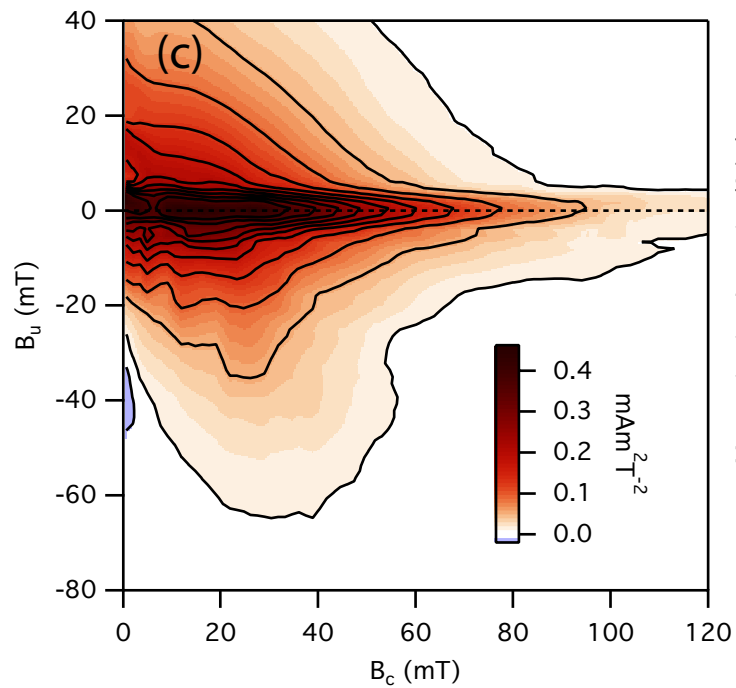
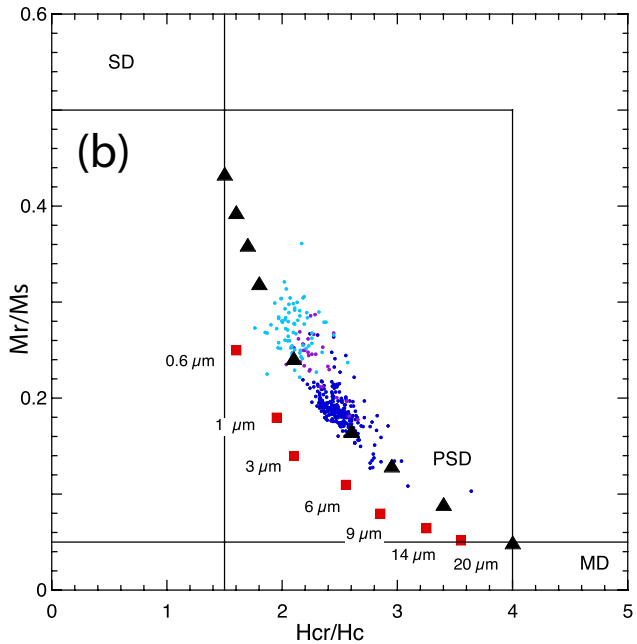
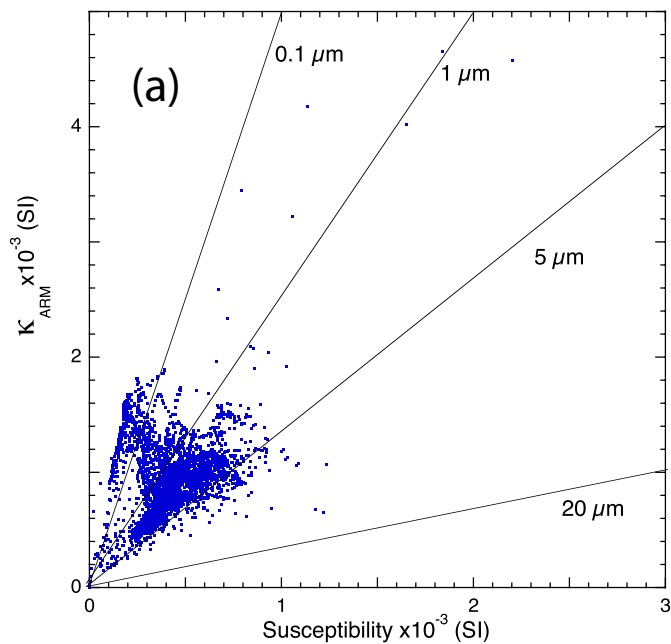


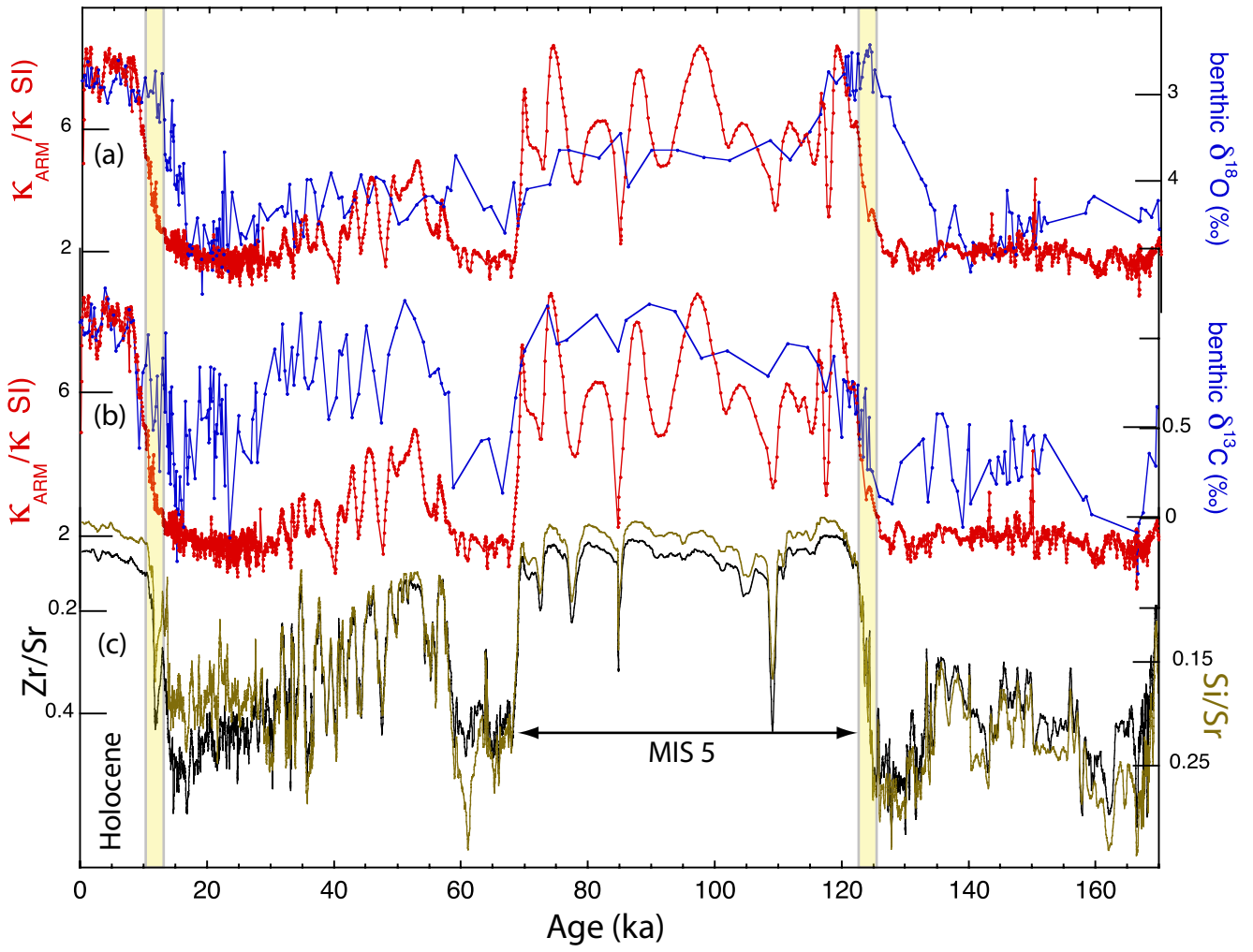


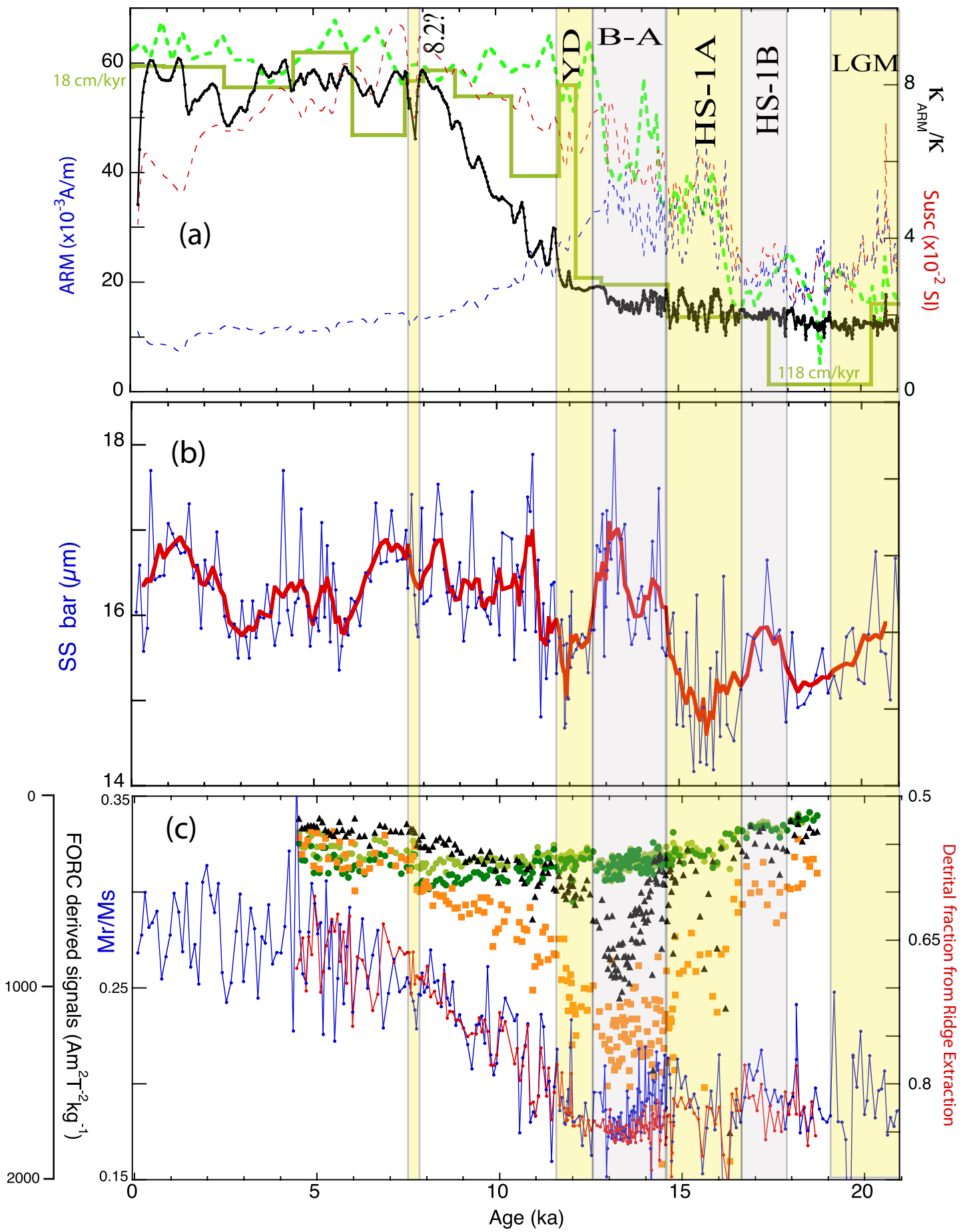


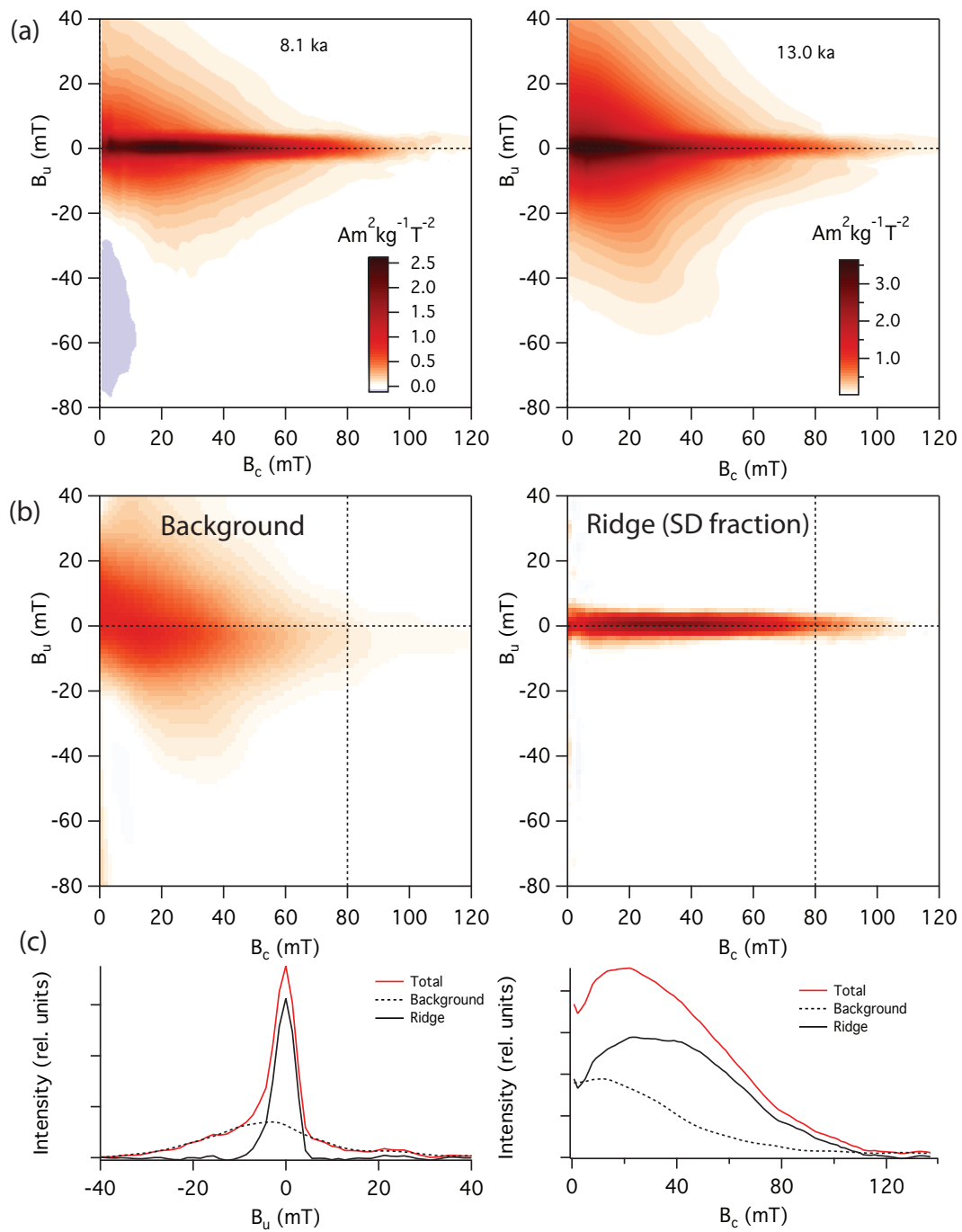


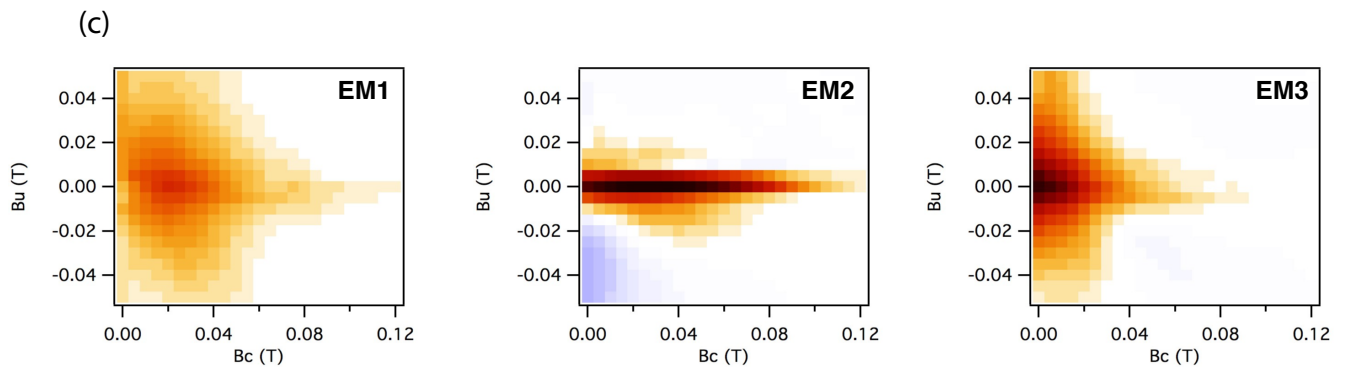
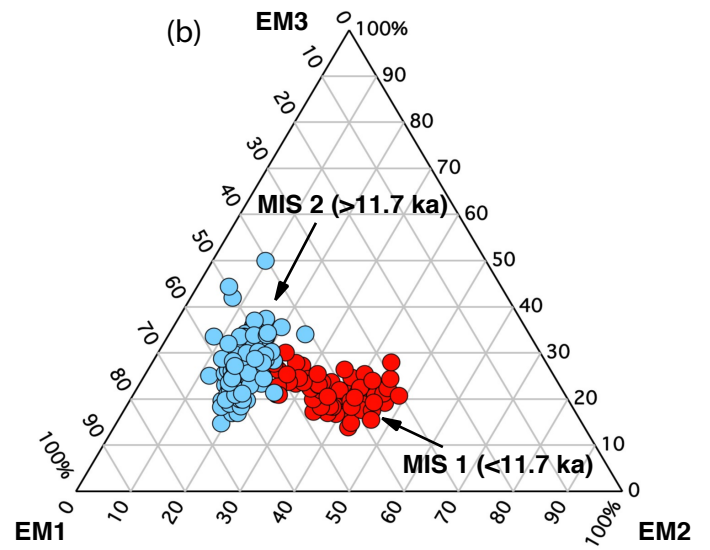
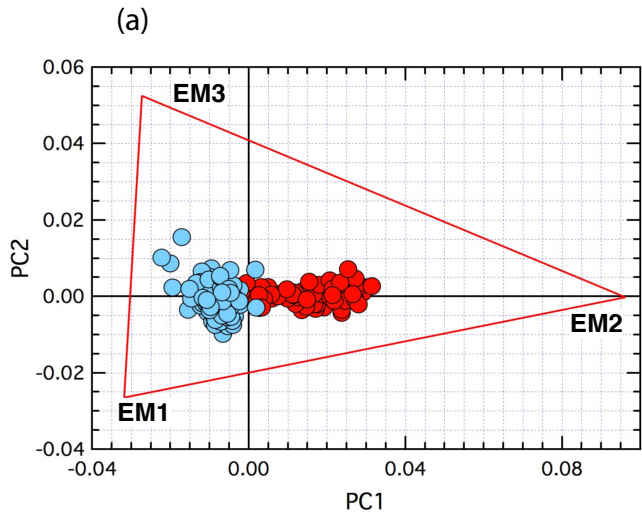


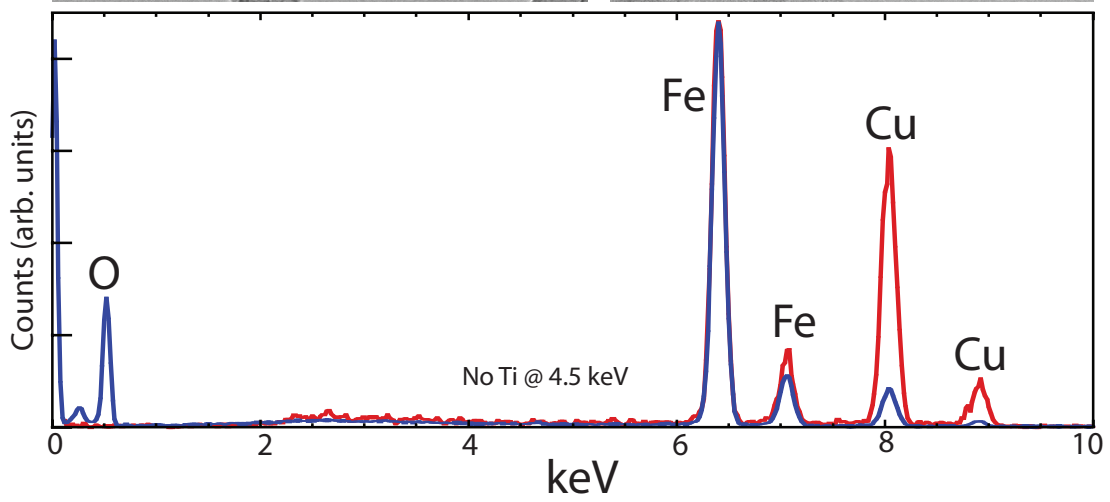
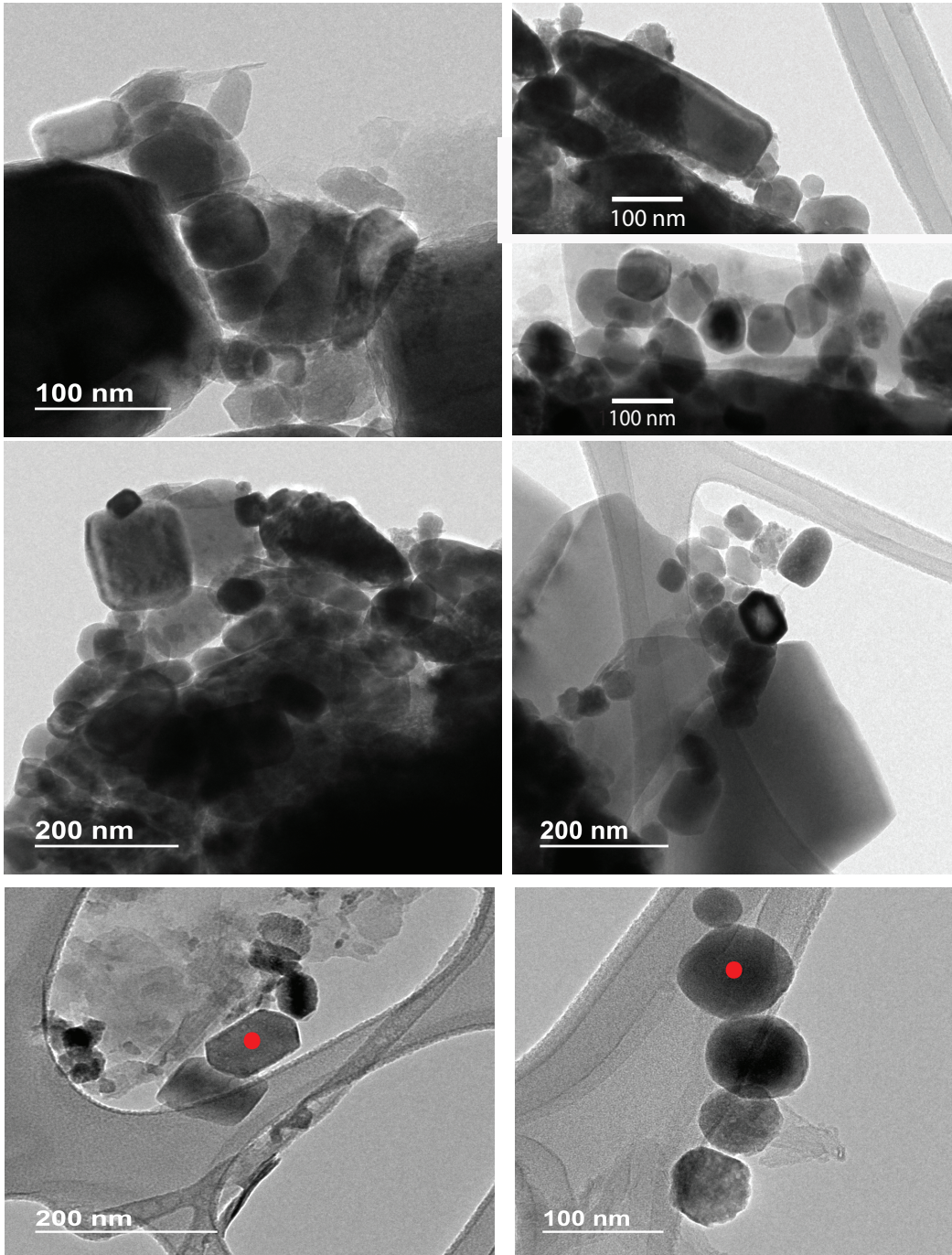












Magnetic record of deglaciation using FORC-PCA, sortable-silt grain size, and magnetic excursion at 26 ka, from the Rockall Trough (NE Atlantic)

J.E.T. Channell¹, R.J. Harrison², I. Lascu², I. N. McCave², F.D. Hibbert³, W.E.N. Austin^{4,5}

¹Department of Geological Sciences, POB 112120, University of Florida, Gainesville, FL 32611 (USA)

²Department of Earth Sciences, University of Cambridge, Cambridge, CB2 3EQ (UK)

³Research School of Earth Sciences, Australian National University, Canberra, ACT 2601, Australia

⁴School of Geography and Geosciences, University of St. Andrews, St. Andrews, KY16 9AL (UK)

⁵Scottish Marine Institute, Scottish Association for Marine Science, Oban PA37 1QA, (UK)

Contents of this file

Figure S1
Tables S1 and S2

Introduction

Additional information related to the age model for Core MD04-2822, supplemental to Figure 2.

Figure S1. Age-depth relationship for Core MD04-2822 with age error estimates.

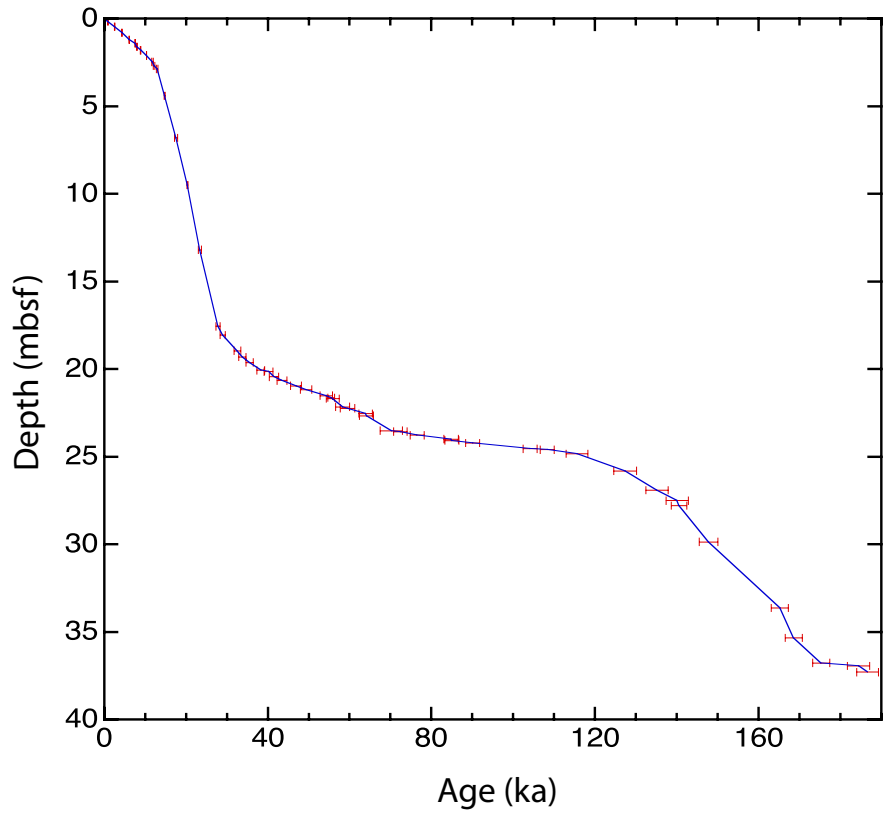


Table S1: Radiocarbon dates used in the construction of the MD04-2822 age model

* calibrated using OxCal (version 4.2; Bronk-Ramsey, 2009) using the Marine13 calibration curve (Reimer et al., 2013)

† calibrated using OxCal (version 4.2; Bronk-Ramsey, 2009) using the Marine13 calibration curve (Reimer et al., 2013) and deposition model in (Bronk Ramsey and Lee, 2013); k parameter of 1 but allowed to vary between a factor of 10^{-2} and 10^2 to allow for changes in deposition.

^(a) The similarity of the radiocarbon determinations results from the biological mixing of sediments (cf. Brown et al., 2001), as such we set the bottom of the surface mixed layer to a depth of 15.5 cm and use an average of these three radiocarbon dates in the age model for MD04-2822 (Table 2, “mixed layer”)

^(b) average (n=6) for the wider region gives a value of $\Delta R = -1 \pm 53$ (Harkness, 1983; Häykansson, 1984; Olsson, 1980)

^(c) for sample SUERC 12920 we use $\Delta R = 700 \pm 500$ for calibration. Austin et al., 1995 suggest $\Delta R = 700$ for the area during the Younger Dryas; we assume similar surface conditions but recognize that ΔR have have been far greater (cf. Waelbroeck et al., 2001) by including a ± 500 year uncertainty

Depth cm	Publication Code	Material dated	Species	Conventional ¹⁴ C (years)	± 1 sigma	$\Delta R \pm 1$ sigma (years)	Calibrated 14C age BP (unmodelled*) (95% range) (years BP)	μ (years)	$\pm \sigma$	Calibrated 14C age BP (modelled†) (95%)(years BP)	μ (years)	$\pm \sigma$
0.5	SUERC 20177 ^(a)	Planktonic foraminifera	<i>G. bulloides</i>	1352	35	$0 \pm 50^{(b)}$	886 to 733	807	41	n/a	n/a	n/a
5.5	UBA 29428 ^(a)	Planktonic foraminifera	<i>G. bulloides</i>	1333	33	$0 \pm 50^{(b)}$	949 to 784	871	43	n/a	n/a	n/a
15.5	UBA 29429 ^(a)	Planktonic foraminifera	<i>G. bulloides</i>	1260	21	$0 \pm 50^{(b)}$	972 to 790	892	46	n/a	n/a	n/a
45.5	UBA 29430	Planktonic foraminifera	<i>G. bulloides</i>	2792	23	$0 \pm 50^{(b)}$	2690 to 2358	2534	91	2680 to 2351	2518	95
80.5	UBA 29431	Planktonic foraminifera	<i>G. bulloides</i>	4311	28	$0 \pm 50^{(b)}$	4605 to 4255	4438	85	4561 to 4270	4422	73
120.5	UBA 29432	Planktonic foraminifera	<i>G. bulloides</i>	5648	26	$0 \pm 50^{(b)}$	6185 to 5911	6052	73	6171 to 5907	6038	82
140.5	UBA 29433	Planktonic foraminifera	<i>G. bulloides</i>	6995	29	$0 \pm 50^{(b)}$	7593 to 7397	7491	50	7576 to 7396	7483	50
160.5	UBA 29434	Planktonic foraminifera	<i>G. bulloides</i>	7539	35	$0 \pm 50^{(b)}$	8146 to 7875	8004	68	8121 to 7865	7984	64
180.5	UBA 29435	Planktonic foraminifera	<i>G. bulloides</i>	8313	33	$0 \pm 50^{(b)}$	9015 to 8645	8857	97	9008 to 8653	8856	101
210.5	SUERC 17731	Planktonic foraminifera	<i>G. bulloides</i>	9552	39	$0 \pm 50^{(b)}$	10569 to 10237	10410	89	10559 to 10234	10392	132
950.5	SUERC 12920	Planktonic foraminifera	<i>N. pachyderma</i> (sinistral)	17200	70	$700 \pm 500^{(c)}$	20611 to 18287	19445	581	20559 to 18604	19553	497

Table S2: Input tie-points used to construct the age model for Core MD04-2822.

Age model constructed using ‘Poisson’ function (deposition model) in OxCal (Bronk Ramsey and Lee, 2013); k parameter of 1 but which can vary between a factor of 10^{-2} and 10^2 to allow for changes in deposition. Age uncertainty estimates for each tie-points, except for radiocarbon dates, are the mean squared estimate of: the reference chronology uncertainty (i.e. NGRIP $\delta^{18}\text{O}$ on the GICC05 timescale, Rasmussen et al., 2014 and references therein; EDC methane record on the AICC2012 chronology, Bazin et al., 2013 and; LR04 $\delta^{18}\text{O}$ stack, Lisiecki and Raymo, 2005) and tuning uncertainties. For tuning to the Greenland ice cores, we use the updated ice core nomenclature (where GI = Greenland Interstadial and GS = Greenland Stadial) and ages (Rasmussen et al., 2014 and references therein). Radiocarbon dates were calibrated using the Marine13 calibration curve (Reimer et al., 2013); $\Delta R = 0 \pm 50$ for all samples except SUERC 12920 where this was increased to $\Delta R = 700 \pm 500$ to account for changes in the glacial surface ocean. The mixed depth was set at 15.5 cm and an average of three radiocarbon dates used (SUERC 20177, UBA 29428, UBA 29429, Table 1). Note radiocarbon dates are reported here as conventional ^{14}C .

* Conventional ^{14}C age (and ± 1 sigma uncertainty)

Depth (cm 1 dp)	Age (ka)	$\pm 1 \sigma$ (ka, 2dp)	Tie-point origin
0	0.000	0.20	Core top
15.5	1.350	0.02	Depth of bottom of mixed layer: average of 3 ^{14}C date (all <i>G. bulloides</i> , Table 1)
45.5	2.792*	0.02	^{14}C date: UBA29430 (<i>G. bulloides</i>)
80.5	4.311*	0.03	^{14}C date: UBA29431 (<i>G. bulloides</i>)
120.5	5.648*	0.03	^{14}C date: UBA29432 (<i>G. bulloides</i>)
140.5	6.995*	0.03	^{14}C date: UBA29433 (<i>G. bulloides</i>)
160.5	7.539*	0.04	^{14}C date: UBA29434 (<i>G. bulloides</i>)
180.5	8.313*	0.03	^{14}C date: UBA29435 (<i>G. bulloides</i>)
210.5	9.552*	0.04	^{14}C date: SUERC17731 (<i>G. bulloides</i>)
246.5	11.703	0.09	Start of Holocene – correlation to NGRIP $\delta^{18}\text{O}$
270.5	12.171	0.04	Tephra horizon: Vedde Ash (I-RYH-I)
287.5	12.896	0.10	GS1 – correlation to NGRIP $\delta^{18}\text{O}$
440.5	14.692	0.13	GI-1e – correlation to NGRIP $\delta^{18}\text{O}$
680.5	17.480	0.33	GI-2.1 – correlation to NGRIP $\delta^{18}\text{O}$
950.5	17.200*	0.07	^{14}C date: SUERC129020N (<i>N. pachyderma</i> (sin.))
1319.6	23.340	0.41	GI2.2 – correlation to NGRIP $\delta^{18}\text{O}$
1756.0	27.780	0.57	GI-3 – correlation to NGRIP $\delta^{18}\text{O}$
1805.4	28.900	0.61	GI-4 – correlation to NGRIP $\delta^{18}\text{O}$
1895.7	32.500	0.77	GI-5.2 – correlation to NGRIP $\delta^{18}\text{O}$
1930.5	33.740	0.83	GI-6 – correlation to NGRIP $\delta^{18}\text{O}$
1962.1	35.480	0.91	GI-7c – correlation to NGRIP $\delta^{18}\text{O}$
2006.6	38.220	0.99	GI-8c – correlation to NGRIP $\delta^{18}\text{O}$
2014.5	40.160	1.09	GI-9 – correlation to NGRIP $\delta^{18}\text{O}$
2044.1	41.460	1.12	GI-10 – correlation to NGRIP $\delta^{18}\text{O}$
2065.6	43.340	1.20	GI-11 – correlation to NGRIP $\delta^{18}\text{O}$

2095.2	46.860	1.33	GI-12c – correlation to NGRIP $\delta^{18}\text{O}$
2116.7	49.280	1.41	GI-13c – correlation to NGRIP $\delta^{18}\text{O}$
2151.6	54.220	1.57	GI-14e – correlation to NGRIP $\delta^{18}\text{O}$
2163.5	55.380	0.81	Tephra horizon: NAAZII
2168.0	55.800	1.62	GI-15.2 – correlation to NGRIP $\delta^{18}\text{O}$
2215.3	58.280	1.72	GI-16.2 – correlation to NGRIP $\delta^{18}\text{O}$
2223.6	59.440	1.75	GI-17.2 – correlation to NGRIP $\delta^{18}\text{O}$
2254.5	63.840	1.70	GI-18 – correlation to NGRIP $\delta^{18}\text{O}$
2352.0	70.150	2.72	Correlation to LR04 $\delta^{18}\text{O}$
2357.3	72.340	1.70	GI-19.2 – correlation to NGRIP $\delta^{18}\text{O}$
2376.8	76.440	1.70	GI-20c – correlation to NGRIP $\delta^{18}\text{O}$
2399.7	84.760	1.71	GI-21.1e – correlation to NGRIP $\delta^{18}\text{O}$
2407.5	84.600	1.70	GS-22 – correlation to NGRIP $\delta^{18}\text{O}$
2412.4	90.040	1.70	GI-22g – correlation to NGRIP $\delta^{18}\text{O}$
2455.4	104.040	1.72	GI-23.1 – correlation to NGRIP $\delta^{18}\text{O}$
2460.1	108.280	1.71	GI-24.2 – correlation to NGRIP $\delta^{18}\text{O}$
2483.3	115.540	2.72	Correlation to LR04 $\delta^{18}\text{O}$
2581.3	127.321	2.72	Correlation to LR04 $\delta^{18}\text{O}$
2691.7	135.072	2.73	Correlation to LR04 $\delta^{18}\text{O}$
2750.8	140.004	2.72	Correlation to LR04 $\delta^{18}\text{O}$
2779.2	140.515	1.90	Correlation to Antarctic (EDC) methane
2986.7	147.720	2.25	Correlation to Antarctic (EDC) methane
3363.5	165.159	2.14	Correlation to Antarctic (EDC) methane
3534.3	168.542	2.04	Correlation to Antarctic (EDC) methane
3677.7	175.269	2.03	Correlation to Antarctic (EDC) methane
3693.2	184.404	2.73	Correlation to LR04 $\delta^{18}\text{O}$
3730.2	186.600	2.72	Correlation to LR04 $\delta^{18}\text{O}$